UNIFORM DUCTILITY OF HIGH CARBON STEELS

UNIFORM DUCTILITY OF HIGH CARBON STEELS

By

MASARU YAMAGUCHI, B. Eng.

A Thesis

Submitted to the School of Graduate Studies

in Partial Fulfilment of the Requirements

for the Degree

Master of Engineering

McMaster University

November, 1971

MASTER OF ENGINEERING
(Metallurgy and Materials Science)

McMASTER UNIVERSITY
Hamilton, Ontario.

TITLE: Uniform Ductility of High Carbon Steels

AUTHOR: Masaru Yamaguchi, B. Eng. (Chiba Inst. Tech., Japan)

SUPERVISOR: Professor G.R. Piercy

NUMBER OF PAGES: (ix); 102

SCOPE AND CONTENTS:

Effect of microstructure on uniform ductility was analyzed by utilizing a fact that uniform ductility is equal to the work hardening coefficient in parabolic true stress-true strain equation. A Hall-Petch relation was found for the flow stress of lamellar and spheroidized high carbon steels. The uniform ductility was formulated as a function of reciprocal flow stress and found to fit the experimental data.

An attempt to interpret the results obtained, based on the scanning and transmission electron microscopy observations, were given.

ACKNOWLEDGMENTS

This work was done under the supervision of Professor G. R. Piercy. The author appreciates his patient guidance over the research.

Helpful discussions on the experimental techniques were given by Associate Professor, Dr. J. D. Embury. The author thanks him.

Appreciation is extended to Dr. G. L. Montgomery, Senior Research Associate, The Steel Company of Canada, Limited, Hamilton, for his helpful discussions on the results.

Appreciation is also given to R. Jarochowicz, former technician in this department, and to M. J. Brown, graduate student.

Precise typing was done by Mrs. Anita Miltimore. The author is very grateful to her.

TABLE OF CONTENTS

LIST OF FIGURES AND TABLES

GENERAL INTRODUCTION

One of the important mechanical properties of mass produced plain carbon steels is their ductility. There are many parameters of ductility which are evaluated by tensile testing at room temperatures. Some of the more commonly used parameters in industrial specifications are:

1. uniform elongation; the total extension from the beginning of deformation to the strain giving the ultimate tensile strength (U. T. S.). (This is also termed uniform extension. The latter is used in the present work.)

2. reduction of area, the ratio of cross sectional area before and after the tensile fracture, at the center of the neck.

3. total elongation; the total extension to fracture divided by the initial gauge length. This includes the uniform extension plus the local extension of the neck from the U. T. S. to fracture.

The hydrostatic pressure applied during uniaxial tension plays an important role on the ductility. Dieter[17] and Rogers[67] cited its effect on the uniform extension is negligible. On the other hand, the reduction of area and the total elongation are very sensitive to the hydrostatic pressure according to Bridgman[11], Davidson and Ansell[15], Dieter[17] and Rogers[67]. The effect of hydrostatic pressure on the parameters of ductility measuring the strain at the neck region, like reduction of area and total elongation, indicates the significant role of voids in these ductility parameters. Thus, extensive studies on behavior of voids are required for understanding these

ductility parameters, in addition to studies on other features of plastic deformation, such as work hardening.

Uniform extension is used as the ductility parameter in the present study because of its relative insensitivity to the shape and size of tensile sample, its ability to be analyzed with the current level of knowledge, and its importance to industry.

The behaviour of voids may not be able to change the overall stress of the uniaxial tensile stress system[67], not local stress, except at the onset of necking.

Possible directions for the investigation of uniform ductility are either through microscopic studies of voids, which are very difficult to relate to tensile testing except with one model of McClintock[53], or through the extensive work done on plastic deformation. Due to complexity and lack of theoretical analysis, the latter direction is taken in the present study on the uniform ductility of high carbon steels. According to the elementary analysis given in Appendix I, the uniform ductility becomes equal to the work hardening coefficient, if the sample obeys a parabolic true stress-true strain relation.

Plain high carbon steels with carbon ranging from .78 wt. % to .95 wt. % and with the structures either lamellar or spheroidized, were examined. Armco iron was also examined for comparison as a single phase polycrystalline material. Ferrite spacing between cementite plates in a pearlite colony of the lamellar steel, and the ferrite spacing between cementite particles located at the grain boundary for spheroidized steels, were taken as the significant microstructural parameters. From now on these will be called the ferrite mean free path and be abbreviated as F. M. F. P.. Scanning and transmission electron microscopes were used to determine the microstructural parameter for lamellar steels. Optical microscopy was used for spheroidized steels. The tensile testing was carried out on the samples after heat treatment and electropolishing.

A Hall-Petch relation was found to be valid for the yield strength and flow stress. The uniform ductility was formulated as a function of reciprocal flow stress and found to fit the experimental data obtained.

Optical, scanning and transmission electron microscopy were used to examine the structure in samples strained to the limit of uniform extension. Results of submicrostructural observations were used to interpret the uniform ductility.

PART I - LITERATURE REVIEW

No physical interpretation of the uniform ductility is given yet. The literature review is directed so that one can interpret the dependence of the uniform ductility on the microstructure. It is based on studies of the

1. initiation of voids in steels

2. effect of microstructure on the work hardening in low and high carbon steels

3. available experimental studies on the effect of microstructure on uniform ductility.

CHAPTER 1

INITIATION OF VOIDS IN STEELS

1.1 Experimental Studies on Void Initiation

It is generally agreed[17, 67, 69] that void formation in two phase materials occurs by fracture of the interface or fracture of hard phase particles. In the Cu-SiO_2 system, Palmer et al[59, 60] used transmission electron microscopy to detect small voids of .015 μ diameter formed at the interface of SiO_2 particles when the sample was deformed in tension by a small plastic strain. When the strain increased, the voids elongated in a direction parallel to the tensile axis. This result can be understood from elastic analysis well reviewed by Mogford[57] and Gurland and Plateau[29], and from Ashby's analysis[4]. The essential results of elastic analysis is that when a spherical particle of high elastic modulus is embedded in the matrix of low elastic modulus, a maximum tensile stress parallel to the applied tensile axis occurs at the interface intersected by a line running through the center of the particle and parallel to the tensile axis. On the other hand, when a void which can be taken as zero elastic modulus is embedded in the matrix a maximum tensile stress parallel to the applied tensile axis occurs at the interface cut by a line drawn through the center of the particle and perpendicular to the tensile axis.

Russian workers[38] stated that voids were observed in a region of high dislocation density even when there were no hard particles. However, their technique of detection is not clear to the author. Rogers[67] also believed that voids could be nucleated in a tangled structure of dislocations

in single phase materials. In such a case, the tangled dislocation structure might generate a very high local stress which is difficult to analyze theoretically.

The increase of volume due to voids formed at plastic strains less than the uniform extension is negligible[67], although it depends on volume fraction of the second phase and the plastic strain, according to Palmer et al[60].

1.2 Theoretical Studies of Void Initiation

(a) Ashby's Theory

Ashby[4] analyzed the problem of inhomogeneous plastic deformation in terms of the behavior of dislocations. His physical model can be interpreted as follows: assume that an isotropic hard particle is embedded in a soft isotropic matrix, which is in uniaxial tension, as in Fig. 1. Referring to this figure, Ashby expected dislocations on the primary slip system in x-y coordinates, making 45° to x'-y' coordinates, to move a long distance and carry the main part of plastic strain. When they pile up against the hard particle, a high local stress is produced in and around the particle. This may produce new prismatic dislocation loops (vacancy type along y' axis and interstitial type along x' axis) on a secondary slip system. If n prismatic dislocations are spaced evenly in a distance λ along the y' axis

$$\sigma_{ten.} \propto \frac{n}{\lambda} = \frac{\gamma \cdot r}{2b\lambda} \qquad (1)$$

where

$\sigma_{ten.}$: tensile stress at the interface, which nucleates subsequent vacancy type dislocations along the Y' axis

γ : plastic strain on primary slip planes

2r : diameter of hard particle

b : Burgers vector of the prismatic dislocations

This predicts a higher tensile stress at the interface when

1. n increases, due to increased plastic strain,
2. particle diameter increases or
3. λ, which for a first approximation is equal to half the interparticle spacing, decreases.

When the $\sigma_{ten.}$, which cannot be relaxed by nucleation of prismatic dislocations becomes high enough, it may be relaxed by other means. If the particle-matrix interface is weak, a cavity may nucleate in the interface along the Y' axis in Fig. 1.

One of the unanswered problems in this model is how the pile-up of dislocations is to be built up at the plastically non-deformable particle to support sufficient $\sigma_{ten.}$ to fracture the interface.

(b) Gurland and Plateau's Theory

Gurland and Plateau[29] demonstrated that a brittle crack expressed by a Griffith type equation was a valid model for void nucleation in a two phase material. Consideration of the geometrical change of elliptical voids could give a formulation of fracture strain as a function of volume fraction of second phase particles. They cited that the latter could explain experimental results of Edelson and Baldwin[20], who showed both work hardening coefficient and reduction of area were a simple function of volume fraction of second phase particles, no matter what were their rigidities and sizes.

Gurland and Plateau[29] assumed that stress in a spherical hard particle embedded in a soft matrix was higher by a concentration factor, q over the applied stress, without any detailed physical argument. If the fracture takes place in the hard particle and the interface is strong a simple energy criterion can be applied.

When elastically stored energy $\frac{(q\sigma)^2}{E} \cdot \frac{2\pi}{3} r^3$ in a hard particle equals the energy required to create new surfaces, $2\pi\gamma_s r^2$, the following

equation becomes valid,

$$\frac{(q\sigma)^2}{E} \cdot \frac{2\pi}{3} \cdot r^3 = 2\pi\gamma_s r^2 \qquad (2)$$

$$\sigma = \frac{1}{q} \cdot \left(\frac{3E\gamma_s}{r}\right)^{1/2} \qquad (3)$$

where

σ: applied tensile stress

E: Young's modulus of the particle

r: radius of particle

γ_s: surface energy of cracked particle

If γ_s = 1000 ergs/cm^2, E = 10^{12} dynes/cm^2, r = .5 x 10^{-4} cm and q = 2.0, it predicts that the fracture of cementite occurs when the applied stress becomes 45 x 10^3 psi. A crack formed in such fashion may run across the particle instantly but may stop as the stress concentration at the crack tip may be readily relaxed by plastic deformation in the soft matrix.

One of the greatest problems in this simple theory is the assumed stress concentration factor, q. It may be difficult to estimate q accurately for the plastic case.

1.3 Plastic Deformation and Fracture of Cementite

(a) Crystallographic Structure and Dislocations in Cementite

The crystallographic structure of cementite is well reviewed by by Barrett and Massalski[6] and Hume-Rothery[36]. It is orthoromic with a = 4.514Å, b = 5.080Å, and c = 6.734Å. Each carbon atom has six Fe atom neighbours and is located at the center of an Octahedra, if the structure is taken as chains of six Fe atoms projected on the x-y plane. The c axis

corresponds to the z axis in cartesian coordinates, as analyzed by Maurer and Warrington[52]. From examination of the x-y plane projection of chains of Fe atoms, Maurer and Warrington proposed the existence of a partial dislocation with Burgers vector $1/2 \langle 111 \rangle$, which was treated as a type of Lomer-Cottrell sessile dislocation. They used this type of dislocation to explain the high dislocation density observed in their experiments on cementite. They also showed that possible types of Burgers vector of dislocations in cementite were $\{100\}$, $\{010\}$, $\{001\}$ and $\{111\}$, and a possible slip plane was the $\{100\}$ plane[3].

By studying a low carbon steel and a spheroidized 1095 steel deformed at 700°C, Keh[41] showed dislocations with Burgers vector $\{100\}$ moved on (001) planes. He also recognized that the cementite contained stacking faults on (001) planes[41]. The dislocation density in cementite in both low and spheroidized high carbon steels deformed at room temperature was negligible, compared to those in the surrounding ferrite[41]. The fracture of cementite is thought to occur by cleavage on (100) planes with very little prior plastic deformation[41].

(b) Mechanical Properties of Cementite

Young's modulus of cementite is reported to be 25×10^6 psi approximately[78], which is almost the same as the value for ferrite. The yield strength of cementite is thought to be 2×10^6 psi[46], which is 100 times larger than that for ferrite. From this strength data, it can be assumed that the cementite deforms up to six percent elastically, if the surrounding soft matrix can support such a high stress[78]. Puttick[62], Butcher and Pettit[13], Embury and Fisher's[21] suggestion that the cementite deformed plastically in room temperature deformation of steels should be noted here.

CHAPTER 2

PLASTIC DEFORMATION OF PLAIN CARBON STEELS

2.1 Plastic Deformation of Low Carbon Steels

Experimental Observations

A typical process of plastic deformation at small strains is the collection of dislocations into clusters. These eventually become cell walls with increasing strain[10, 18, 56]. During this process, experimental results showed[8, 23]

$$\sigma_{fl} = \sigma_i + \alpha G b \cdot \sqrt{\rho_{av}} \qquad (4)$$

where

σ_{fl}: flow stress at which the average dislocation density, ρ_{av} was measured

σ_i: frictional stress

α: experimental constant expressing the efficiency of strengthening by dislocations

If σ_i and α do not depend on the grain size[18], the only effect of grain size on the flow stress at small strains, say less than 10% occurs through ρ_{av}. Keh and Wissman[40], Dingley and McLean[18], Evans and Rawlings[23] showed that mobile dislocations combine with immobile dislocations to build up the tangled dislocation structures. During the formation of the tangled structure some dislocation annihilation has to be expected[71]. Thus the ρ_{av} may not equal the total dislocation density, ρ.

Experimentally, the Hall-Petch type relation for low carbon steel has been proposed by Armstrong et al[2] and Armstrong[3]. They[2] showed that the Hall-Petch relation is not only valid for small strains but also for large strains, where the cell walls sub-divide the original grains. There was an attempt to correlate ρ_{av} with the sub cell size by Holt[32]. He predicted the cell size proportional to reciprocal square root of dislocation density. Substituting the sub cell size to the experimental relation given by equation (4), as he did, gives an expression that the flow stress is proportional to reciprocal sub cell size. Langford and Cohen[45] showed experimentally that the flow stress is proportional to the reciprocal sub cell size. They controlled the sub cell size by heavy deformation given by swaging. Their result seems to agree with Holt's prediction. However Embury and Fisher[21], and Embury et al[22] gave the Hall-Petch relation for the sub cell size, whose experiment was done prior to Langford and Cohen's. The later results contradict Holt's prediction. As there is no evidence that the accumulated dislocations can only be accommodated by decreasing the sub cell size, which indicates they can also be accommodated by increasing the misorientation angle, it may yet be difficult to conclude that Holt's prediction is valid.

2.2 Experimental Observations of High Carbon Steels

(a) Effect of Microstructures on Strength

About 30 years ago Gensemer et al[26] studied the effect of microstructure on the lower yield stress of a wide variety of steels; low carbon, high carbon, lamellar and spheroidized, and showed that the yield stress was inversely proportional to the mean ferrite size using a logarithmic scale; where the mean ferrite size is the mean uninterrupted straight line through the ferrite for the spheroidized steels and mean interlamellar spacing

for the lamellar steels. Their results were confirmed later by Roberts et al[65] and Turkalo and Low[77].

Hyam and Nutting[37] studied the effect of microstructure of spheroidized steels on the Vickers hardness and found that the hardness depended on the mean ferrite grain diameter. Letting the Vickers hardness represent a parameter of flow stress, their results also show that the flow stress is governed by the mean ferrite grain diameter.

(b) X-ray Studies

Wilson and Konnan[78] measured lattice strains in cementite by determining the change in Bragg angle. Although some doubts in their results still remain, one of the important suggestions is that in spheroidized high carbon steels, elastic stress at the cementite and ferrite matrix was built up rapidly with strain in the first several percent of strain and reaches saturation. In the cementite particle, a tensile stress was built up in the applied tensile direction, which was counterbalanced by a compressive stress in the adjacent ferrite matrix. In the direction perpendicular to the applied tension, a compressive stress was formed in the cementite particle and a tensile stress in the adjacent ferrite. Since the work hardening in ferrite is produced by dislocation interactions, well tangled dislocation structures might be formed at the cementite particle. It could be expected that nucleation of a large number of dislocations occurs in such highly stressed regions. These will carry the local plastic strain which contributes to subsequent work hardening, and reduces the stress concentration at the particles.

2.3 Theoretical Studies of Two-Phase Materials

(a) Classical Theories

There are three principal classical theories. They are those propose by 1) Mott and Nabarro[34], 2) Orowan[34], and 3) Fisher, Hart and Pry[24].

Essential feature of Mott and Nabarro's theory[34] is that when a dislocation is moving through the forest of hard coherent precipitates, the stress required to pass through them depends on the critical radius of curvature of the dislocation.

Orowan's theory proposed that when a dislocation moves through the forest of particles, the dislocation line bulging between the particles leaves a dislocation loop around the particle. The predicted yield stress is inversely proportional to the particle spacing.

Fisher, Hart and Pry[24] extended Orowan's model. They proposed that strengthening by the particles was also due to the back stress from dislocation loops accumulated around the particles.

None of these theories is directly applicable to the case of spheroidized steels, in which coarse spheroidized particles are at the grain boundaries. A dislocation moving through the particle or around it terminates at the grain boundary.

(b) Ashby's Theory

Recently Ashby[5] proposed a theory for plastic deformation of two-phase materials. Essential features of his theory are that a rigid second phase particle does not deform during plastic deformation.

For continuity of the material near the rigid particle-matrix interface, extra strain is necessary. This extra strain is supplied by introducing extra dislocations termed "geometrically necessary dislocations" after Cottrell[14], which may be prismatic loops of interstitial or vacancy type, as is illustrated in Fig. 1. From a Burger's circuit construction for a particular slip system of the soft matrix near the rigid particle, he derived the density of "geometrically necessary dislocation", ρ_G to be inversely proportional to the spacing between the particles. This argument was extended to lamellar structure of rigid and soft phases and he arrived at a similar expression

$$\rho_G = \frac{2\gamma A}{b\lambda} \qquad (5)$$

where

γ: shear strain

b: Burger's vector

λ: spacing of rigid phase

A: numerical constant

It is valid to let $\rho_G = \rho_{av}$ for small strains (which is the case of Ashby's "one parameter work hardening theory") and to utilize equation (4), which then gives a Hall-Petch type expression for the flow stress, σ_{fl}

$$\sigma_{fl} = \sigma_i + \alpha G \sqrt{2b\gamma A} \cdot \frac{1}{\sqrt{\lambda}} \qquad (6)$$

In equation (6), it is assumed that no slip and no fracture occur at the particle interface and that no interaction occurs between the two types of dislocations, "geometrically necessary" and "statistically necessary", where the latter is the term used for dislocations which accumulate during plastic deformation of a pure single crystal. The numerical constant in the equation (6) is one forlamellar structure and may be three for spherical particles and eight for equiaxed particles. The equation (6) predicts that the Hall-Petch slope may be higher in spheroidized steels. Here it may be valid to assume that the F.M.F.P. is equal to the spacing of rigid particles (inter-particle spacing).

CHAPTER 3

EFFECT OF MICROSTRUCTURE ON WORK HARDENING COEFFICIENT

3.1 Experimental Studies

(a) Stress-Strain Relation

For steels, the true stress-true strain curve can be expressed by a parabolic equation when the applicable strain range is limited. Morrison[58] and Kleemola[44], for example, showed that the applicable strain range was from e = .08 to the onset of necking for low carbon steels. For high carbon steels, lamellar[26] and spheroidized[26, 78] a parabolic stress strain relationship was confirmed in a strain range after small plastic strain to the onset of necking.

(b) Low Carbon Steels

Morrison[58] proposed grain size as the significant microstructural parameter for the work hardening coefficient in low carbon steel and showed that the larger the grain size, the larger was the work hardening coefficient. To a first approximation, the work hardening coefficient is equal to the uniform extension[7, 19], as outlined in Appendix I. Supporting evidence is given in Dingley and McLean's paper[18]. On the other hand, there are a few papers stating there is no effect of grain size on the uniform extension. For example, Gladman et al[28] cited that the maximum uniform extension, defined by a method similar to the intersection method given in Appendix I, was not influenced by grain size. Their maximum uniform extension was determined by assuming the work hardening rate ($d\sigma_{\psi}/d\varepsilon$) is a linear function of ε^{-1} and not assuming the parabolic σ_{true} - ε relation which was the case in Morrison's

experiments[58].

Another contradicting experiment was that by Kleemola[44]. He studied the effect of microstructure on mechanical properties of low carbon steels, a half of which contained .05%C, 1% Cu and 1% Ni. He found no effect of ferrite grain size on the work hardening coefficient. However, his microstructure was not well controlled as it was in Morrison[58], and Dingley and McLean's[18] experiments. For plain low carbon steel, he deformed by hot rolling and followed by air cooling, where the finishing temperatures were lower than the A_3 temperature. For alloyed low carbon steel, he aged it at 500°C for 80 mins. In his experiments, what was actually governing the work hardening coefficient was not necessarily the ferrite grain size but might have been the sub cell size in plain low carbon steel and the interparticle spacing in alloyed low carbon steels. Additional comprehensive electron microscopic studies on the dislocation sub structure before the tensile test are required before proper interpretation of Morrison's[58] and Dingley and McLean's[18] experiments can be made.

(c) High Carbon Steels

Gensemer[27] showed that for a wide variety of microstructures; pearlite, hypo eutectoid pearlite and spheroidized high carbon steels, the work hardening coefficient was related to the yield stress. The lower the yield stress, the higher is the work hardening coefficient. Gensemer's arguments were supported recently by Blickwede[7] and Duckworth and Baird[19]. Rosenfield and Hahn[68] formulated the work hardening coefficient, n as a function of σ_Y experimentally by using a simple expression

$$n = \frac{\psi}{\sigma_Y} \qquad (7)$$

They cited the lower the yield stress, σ_Y, the larger is the work hardening coefficient, n, for a wide variety of steels at different temperatures from 77°K

to 293°K and at different strain rates from 10^{-4} to 10 per sec. The constant, ℓ in equation (7) only depends on carbon content and type of microstructure [69].

SUMMARY

A possible way to understand the uniform ductility became clear from an equality between the uniform ductility and the work hardening coefficient under parabolic true stress-true strain relation.

It was shown that the well studied Hall-Petch equation of the flow stress for low carbon steels can be extended to the high carbon steels.

It was understood that the inhomogeneous deformation mode which gave high long range stress by the dislocation tangles in the soft matrix near the embedded particles might be one of the important factors controlling the uniform ductility of high carbon steels.

PART II - EXPERIMENTS

A commercial music wire QQW470, which had carbon content near the eutectoid composition, was used as the initial material. Two principal structures, lamellar pearlite and spheroidized cementite were produced by heat treatment. Tensile tests were performed at room temperature. Scanning electron microscopy and optical microscopy with high magnifications were used to determine F.M.F.P. for lamellar and spheroidized structures. Transmission electron microscopy was used to examine dislocation structures before deformation and after the uniform extension.

It was found that the Hall-Petch equation was valid for the flow stress, and a parabolic expression was valid for the relation between true stress and true strain. From these results, the uniform ductility has been analyzed in terms of work hardening models. One interpretation based on observations of dislocation structures is given.

CHAPTER 4

EXPERIMENTAL PROCEDURES

4.1 Preparation of Tensile Test Samples

(a) Chemical Composition

Commercial eutectoid steel, QQW470 of one quarter inch diameter was used as the initial material for both lamellar and spheroidized steels. Armco iron of one half inch diameter rod, commercially available, was used for the low carbon steel. Chemical analyses are given in Table 1. The high carbon steel contained a negligible chromium content; less than .025 wt.%. This means that the spheroidized structure produced was not controlled by the strong carbide former, chromume, which stabilizes the sub structure in quenched martensite[1]. The carbon content of tensile sample from each heat treated batch was analized, because the heat treatment gave a slight decarburization. These are given in Table 2. The carbon contents in the original material were .830 wt.% and .957 wt.% for groups 1 and 2 respectively. It can be understood that decarburization was taking place during the heat treatment for both lamellar and spheroidized steels.

(b) Outline of Sample Preparation

Lamellar structures were produced mainly by isothermal heating. For spheroidized structures the quench - annealing technique was applied to provide a fast uniform distribution of cementite particles.

Basic steps for production of the structures were as follows:

1. For lamellar steel
    1. as received bar was machined to tensile sample size

2. heat treated by either isothermal heating or continuous cooling followed by very slow cooling.
3. polished the surface of the sample with sand paper No. 400 with extreme care so as not to put any excessive load on the sample.

Thus for lamellar steels no heat treatment was given after the lamellar structure was produced.

2. For spheroidized steel
   1. as-received bar was cut into pieces, two inches long.
   2. heat treated by austenitizing, oil quenching, sub zero treatment and spherodization annealing.
   3. machined, making tensile test specimens and polished by sand paper No. 400 with extreme care.
   4. annealed in vacuum at 600°C for 30 mins. with subsequent furnace cooling.

For spheroidized steels, the specimens were machined and annealed after producing the microstructures.

3. For Armco iron
   1. as-received rod was swaged to 1/4 inch diameter, cut into pieces two inches long and machined, making tensile test samples.
   2. heat treated by austenitizing and furnace cooling.

For Armco iron, the microstructure was produced after the machining.

(c) Heat Treatment

The aim of heat treatment was to control the minimum width of ferrite, i.e. ferrite mean free path (F.M.F.P.) in different structures.

Schematic representation of the heating cycle for each batch of samples used is shown in Figs. 2A, 2B, 2C, where temperature and time in the diagrams were those actually measured.

For fine lamellar steels, LA, LB, LC and for all spheroidized steels, pot type furnaces were used. The salt baths were made up with the following approximate compositions:

	NaCl	KCl	$BaCl_2$	$CaCl_2$
for austenitizing	25%	20%	55%	-
for isothermal transformation	15%	25%	45%	25%

A layer of graphite powder was put on the molten salts to reduce decarburization.

1. Lamellar Steel. The main purpose of the heat treatment for the lamellar structures was to obtain different interlamellar spacings. To avoid spheroidization of the lamellar steel, the maximum isothermal annealing temperature used was 700°C. The minimum transformation temperature used was 600°C which was a practical lower limit at which pearlite forms. For samples, LD, LE, LF, LG, a vacuum furnace (10^{-4} mmHg) was used for austenitizing and subsequent transformation. Samples LD, LE were transformed during continuous cooling. The heating cycle is given in Fig. 2A. For fine lamellar steels, LA, LB, a pot furnace containing salts shown previously was used. About 10-12 min. was needed to bring the temperatures of the sample from austenitizing to isothermal transformation temperatures for LF and LG in the vacuum furnace. About 1 - 2 sec. was needed to move the sample from the hot bath, in which it was austenitized and furnace cooled to 800°C, to the isothermal transformation bath kept at a given temperature. Time for completion of the transformation was determined from the TTT curve for steel containing a similar amount of carbon and manganese[54].

The cooling rate was approximately 1°C per min. for LD, LE, LF, and LG.

For fine lamellar steel, it was approximately 2°C per min., which was obtained by putting the isothermally transformed sample into a can containing graphite powder, which was previously heated to 580-590°C, and placing the covered can in the pot furnace, after which the power was immediately switched off. The temperature in the salt baths and in the graphite powder was continuously measured.

2. Spheroidized Steel. The aim of spheroidization is to produce different ferrite spacing. For fast heat treatments to produce spheroidization of cementite, a martensitic quench and annealing technique was used, instead of direct isothermal annealing to decompose a pearlitic structure. Fig. 2B shows schematically the heating cycle for all samples spheroidized. The fraction of sample transformed to martensite is influenced by the prior austenite grain size and cooling rates. For all samples, both spheroidized and lamellar steels, the same austenizing conditions were applied. The austenizing temperature was 900°C and the time was three hours. From a preliminary test, this gave the austenite grain size, ASTM No. 4 (91 μ diameter) which was fairly large. To avoid quenching cracks yet provide fast cooling rates, a mineral oil with mild agitation was employed. Micro Vicker's Hardness of as quenched samples using a 136" diamond indentor gave a hardness of 1500. The samples were subsequently sub zero treated by dipping them in a dewar containing alcohol and dry ice at -76°C. This completed the martensitic transformation and produced a uniform structure before tempering. Various annealing temperatures and times were used to obtain different F. M. F. P. as shown in Fig. 2B. All temperatures and times used for the spheroidization annealing were sufficient to produce recrystallized ferrite by the precipitation of cementite from the martensite. A vacuum furnace (10^{-4} mmHg), in which the temperature was checked by an Alumel-Chromel thermocouple was used for these spheroidization anneals.

This treatment was aimed to produce a microstructure before tensile testing that did not contain any dislocation sub structures between the cementite particles in the ferrite matrix.

3. Armco Iron. Fig. 2C shows the heat treatment for Armco iron schematically. After reducing the diameter of rod to one quarter inch with a combination annealing and swaging, and cutting into pieces of two inch length, the Armco iron was machined into tensile samples. Subsequently the heat treatment was carried out by austenitizing at 1000°C (one hour for Armco A and two hours for Armco B) and furnace cooling (1.5°C per min.). The vacuum furnace used for the spheroidization was again used for the above heat treatment.

(d) Polishing of Tensile Samples

All tensile samples were electrolytically polished to reduce any surface flaw in the gauge length, which might cause a stress concentration. The polishing conditions were the following:

1. solution[9]: 133 cc acetic acid (purity 99%)
   7 cc H_2O
   25g chromic oxide
2. voltage: 18 - 22V
3. temperature: 13 cc - 18 cc
4. cathode: a band of stainless steel

The sample was kept rotating at the center of the bent stainless steel band that formed the cathode in order to decrease the Fe ion concentration gradient in the solution near the anode. The electropolishing time was determined by observation of the sample surface. The sample was rinsed in two separate alcohol baths and kept in the alcohol until tensile testing.

4.2 Procedure of Tensile Test

A floor type Instron testing machine was used to test the samples. The load on the sample was measured by elastic strain gauges in the Instron load cell. Its signal was amplified, rectified, and sent to the recording units. The strain in the sample gauge length was monitored by a standard extensometer of one inch gauge length, placed on the sample with clips. Its electrical output, which was proportional to the change of distance between the clips, was transmitted to the recording chart drive unit. Thus, simultaneous measurement of both load and sample extension were recorded. Under the actual testing conditions, proportionality between displacement of strain gauge clips, measured by a micrometer, and recording chart movement was checked. It was found to be accurate within the reading errors of $\pm$ .0025 strain.

The size of the tensile sample used for all microstructures is illustrated in Fig. 3. The diameter of the sample was 1/8 inches and the gauge length was 3/2 inches so that the 1 inch gauge length extensometer could be accommodated. The gauge diameter of each sample was machined to a uniformity of $\pm$ .00025 inches. A special grip system shown in Fig. 4 was used to produce self axial alignment of the sample during the intial loading. The lower grip was held rigidly by a fixture attached to the moving crosshead, as illustrated in Fig. 5. The upper grip was connected with a pin to the extension rod of the load cell.

The tensile test was done at room temperature (20 - 26^{o}C) using the slow crosshead movement of 0.02 inches per min. It has been observed that the spheroidized sample with fine structure and most lamellar steels broke immediately after the maximum load was reached. For coarse spheroidized materials, relatively large extensions, whose magnitude depended on the interparticle spacing, were developed during the necking. To calculate the stress at an instantaneous strain, the cross sectional area of samples before the test was determined from two measured diameters taken at three locations

in the gauge length.

4.3 Preparation of Thin Foils

Thin foil specimens used to examine the structures before tensile testing and block specimens used for microstructural observations by either optical or scanning microscopy, were all taken from the same region of the tensile sample. Thin foil specimens used to examine the dislocation structure in sample deformed by uniform extension were cut from regions away from the neck and grip shoulder of the tensile sample. They were usually cut parallel to the tensile axis, but in some cases (Armco B and SF) they were also cut perpendicular to the tensile axis. The following steps were taken to prepare thin foils for observation using transmission electron microscopy.

1. cut a block sample of thickness, .02 - .05 inch by jewelers saw
2. mechanically polish with emery paper using water lubricant to a thickness less than .005 inch, using a hardened rubber block to hold the specimen
3. chemically polish in a solution composed of
   55^{cc} HF (purity 52%)
   95^{cc} H_2O_2 (purity 30%)
   at room temperature for 1 - 3 min.
4. electrolytically polish under the following conditions:
   solution: 95^{cc} acetic acid (purity 99%)
   10^{cc} perchloric acid (purity 71 - 73%)
   25^{cc} Ethanol (purity 99%)
   cathode: stanless steel sheet
   temperature: $15^{o}C$ - $25^{o}C$
   applied voltage: 14V - 18V
   current density: kept in a range between A and B in Fig. 6 by reading the ammeter

A similar solution, from which the above was newly developed, was shown by Brammer et al[8]. Extreme care was taken during all parts of the preparation to not induce dislocations or make them move. A check for this was made on samples strained to the uniform extension. An aging treatment (15 mins. at 80°C) of SF was given to pin the dislocations immediately after the strain. A thin foil of non aged SF was observed within five hours after the tensile test. No noticeable difference was observed. All thin foils shown in the thesis were observed at least two weeks after the tensile test. It was expected that all dislocations were effectively locked, although they could escape from the thin foil and thus the structures could be drastically rearranged as cited by Ham[31]. All transmission electron micrographs were taken at 100 kV. Each time a diffraction pattern was taken, the alignment of the electron beam was checked.

4.4 Preparation for Void Observation

The voids formed during uniform extension in different microstructures were observed using the optical microscope, and scanning electron microscope. Each specimen was cut from a section away from the neck and the shoulder regions to ensure that the specimen investigated had received the uniform extension. The prepration technique was the same as that described for the observation of microstructures before the tensile test. Care was taken to not confuse voids with non metallic inclusions on polished and etched surfaces. An alternative prepration technique proposed by Tanaka et al[75] was used on some specimens for void observation. Following tensile deformation, a small sharp notch was made in the gauge of the sample away from the necked region by eccentric mounting and cutting on a lathe. Care was taken not to impose any excessive stress on the specimen. The specimen was then cooled in liquid nitrogen and fractured in a Charpy impact machine.

4.5 Measurement and Results of Microstructures

Measurements of F.M.F.P. were made by either electron microscopy for lamellar steels or optical microscopy for spheroidized steels and Armco iron.

Samples of two orientations, one, a lognitudinal section parallel to the rod axis, and the other, a transverse section perpendicular to the rod axis, were cut from the undeformed grip regions of tensile samples, LB, LD, LG, SB, Armco A and Armco B. For the other batch of heat treatments, the samples for microstructural examination were similarly cut but from the gauge length region of spare undeformed tensile samples. Thus two sections for each batch of heat treatment were prepared for microstructural measurements. All sections were mechanically polished, finished with a lubricated abrasive of 0.3 microns alumina and etched by one percent nital, carefully avoiding oxidation during and after the etching.

(a) Lamellar Steel

A Cambridge Stereo Scan electron microscope was used to estimate the F.M.F.P., in pearlite. If the pearlite colonies were randomly oriented to the polished and etched surface and if in each pearlite colony, the cementite plates lie parallel to each other with a constant spacing, then the minimum spacing observable is the true lamellar spacing. The interlamellar spacing was measured using the following procedure. The polished sample was wetted by methanol, then carefully etched by applying a small cotton ball wetted with one percent nital and then diluting the acidity on the surface by pouring methanol over it. The whole block of plastic mold in which the samples were mounted, was then dipped in fresh methanol, cleaned using an ultrasonic vibrator and dried by compressed dry air. This reduced oxidation of the etched surface. Three scanning microscope pictures from 20,000 to 50,000 magnification were taken on each polished section. Thus, six pictures showing pearlite colonies

of minimum spacing between cementite plates were taken from each heat treated batch. A typical picture is shown in Fig. 7. Each picture contained 9 - 14 cementite plates, whose spacing was measured. The results are given in Table 3. This technique was used by Brown and Ridley[12]. From the edgewise growth model of a lamellar structure, like those reviewed by Hull and Mehl[35], it was expected that when the interlamellar spacing increased, the thickness of cementite plate also had to increase, or a new cementite plate had to be formed between the extending cementite plates as cited by Sundquist[74].

If the latter did not happen the minimum ferrite spacing between the cementite plate could be found from the measured thickness of the cementite plate.

From transmission electron microscopy pictures of the undeformed structure, the minimum thickness of the cementite plates was estimated from measurement of two cementite plates and plotted against the interlamellar spacing measured by the scanning electron microscopy in Fig. 8. From Fig. 8, the F.M.F.P. was estimated and listed in Table 3. A typical transmission electron micrograph is shown in Fig. 9.

An alternative technique using optical microscopy applied by Gensemer et al to determine interlamellar spacing was proposed by Pillissier et al[61] about 30 years ago.

(b) Spheroidized Steel

It was rather tedious to measure the ferrite grain diameter in spheroidized steels in electron microscopy at a statistically significant level. Optical microscopy, which covered larger areas of the specimens, was used. A typical structure of spheroidized steels is shown in Fig. 10. As described later, in spheroidized steels the F.M.F.P. observed is taken to be the ferrite grain diameter, which was suggested by Hyam and Nutting[37] first and then by Turkalo and Low[77]. Hyam and Nutting[37] and Turkalo

and Low[77] employed Smith's derivation[73] of the grain growth model for the two phase materials. An essential aspect of Smith's grain growth model[73] is that during the annealing, the driving force for the grain growth is equal to the restraining force for each particle. The resulting formula for constant particle diameter is

$$\frac{\lambda}{r} = \frac{4}{3V_f} \qquad (8)^*$$

where λ: diameter of growing grain

r: radius of particle

V_f: volume fraction of particles.

Using the value of r and V_f from quantitative metallographic techniques described in Appendix II, the diameter of ferrite grain, λ was determined. These are listed in Table 5. According to a quantitative metallographic technique first proposed by Fullman[25], and reviewed by Rostoker and Dvorak[70] and De Hoff[16], the mean ferrite spacing between cementite particles, which did not include the existence of grain boundaries, is

$$\lambda_{ini} = \frac{3\pi N_A - 8N_L^2}{3 \cdot \pi \cdot N_A} \cdot \frac{1}{N_L} \qquad (9)$$

where

λ_{ini} = mean ferrite spacing between the particles

N_L = number of particles per unit length

N_A = number of particles per unit area

The derivation of the above equation is given in Appendix II, following Fullman's analysis[25]. To find N_A and N_L, six highly magnified optical micrographs were taken for each heat treated batch; three from the polished

* The numerical constants for equation (8) given by Smith[73] are not correct.

longitudinal section and three from the transverse section. The magnifications were x1000 for SE and SF, x1600 for SB, SC and SD, and x2000 for SA. About 300 - 900 particles were counted for the N_A. Three lines with angular changes of 45^o were drawn on each micrograph and N_L was determined by counting the total number of particles intercepted by known length of lines. The number was about 35 to 75 particles. The results are listed in Table 4, together with other parameters r and V_f. From a comparison between Tables 5 and 4, it can be concluded that ferrite grain diameter based on Smith's model for fine structures like those of SA and SB, is larger than the corresponding values of mean ferrite spacing based on Fullman's analysis, given in Table 4. This aspect was pointed out by two papers of Hyam and Nutting[37] and Turkalo and Low[77] This may be due to an inadequate assumption in the grain growth model. During the early stage of spheroidization, the so called"steady state spheroidization model", i.e. growth of cementite particles driven by the different radius of curvature of the particles, may not yet be established. Because of this uncertainty, the mean ferrite spacing based on Fullman's analysis, given in Table 4, is used for the F.M.F.P..

(c) Armco Iron

If the grain size in a given polycrystalline material is constant, it can be determined by measuring the number of ferrite grains per unit area, as reviewed by Rostoker and Dvorak[70] and shown in Appendix II. From Appendix II

$$\lambda = 1.25 \cdot \frac{1}{\sqrt{n_A}} \qquad (10)$$

where λ is the grain size and

n_A is the number of ferrite grains per unit area

Six values of n_A have been measured from micrographs at x100 of six Armco A specimens.

For Armco B the sub cell size was estimated from the optical micrographs. In Fig. 11B, regular etch pit traces in the large ferrite grains indicate a sub cell structure that is not present in Armco A as noted in Fig. 11A. These traces were taken as the sub cell size which was used for F.M.F.P. in this material.

The results are listed in Table 6.

CHAPTER 5

RESULTS OF EXPERIMENT

5.1 Results of Sub-Structure Observation

(a) Sub-structures before Tensile Test

1. Lamellar Steel

The scanning and transmission electron microscopic observation confirmed so called "growth faults" in the lamellar structures. It was assumed for determination of minimum F. M. F. P. in the lamellar steels, that cementite plates in a pearlite colony were ideally parallel. This was true for a first approximation, according to the scanning microscopic observations done. However, it was not true at a local sub microstructural scale. It was often observed in the thin foil transmission microscopy that the cementite plates were discontinuous in a pearlite colony. Some examples are shown in Figs. 12 and 13. In both structures, dislocations, some of which are coming out from the ferrite-cementite interface (in Fig. 13) and some of which lie parallel to the cementite plates, are possibly due to thin foil preparation. A grain boundary running across the pearlite colony, a structure often observed, is also seen in Fig. 12. No sub cell walls were observed in the ferrite region sandwiched by the cementite plates in an undeformed sample. Observations by optical microscopy indicate that it is reasonable for a first approximation to assume that cementite plates in a pearlite colony are parallel.

Puttick[62] observed slip at the cementite plate-ferrite interface in a deformed pearlite structure, which suggested that the interface was incoherent and might be weak.

2. Spheroidized Steel

Hyam and Nutting[37] first attempted to discriminate between the effect of ferrite grain size, which was controlled by the spheroidized cementite particles in accelerated spheroidization annealing, and the effect of ferrite grain boundaries or sub grain boundaries on mechanical properties. In all spheroidized steels, cementite particles were predominantly located at the "high angle grain boundaries". According to the similarity in microstructures between the present study and those by Hyam and Nutting[37] and Turkalo and Low[77], who all studied spherodized microstructures by replica techniques, their unidentified "ferrite grain boundaries" were "high angle grain boundaries". This conclusion was reached in the present study from the following observations:

1. the intensity of transmitted electrons was much different from one ferrite grain to another (Figs. 14 and 15)

2. fringe contrasts were seen at the boundaries (Fig. 14)

3. the zone axis of one grain was at a large angle from that of neighbouring grains, as demonstrated in Fig. 15.

Inside a grain surrounded by the large angle boundaries, there were no dislocations and no sub cell structures, as shown in Fig. 14. This is probably due to recrystallization occurring after the cementite precipitated.

3. Armco Iron

In the measurement of ferrite grain diameter of Armco B, the regular etch pit traces were observed. Fig. 16 shows a structure, which looks like a sub cell wall, running from a high angle grain boundary. One estimate shows an agreement between a largest spacing of structure like that in Fig. 16 and the largest spacing of etch pit traces (Fig. 11B). No spheroidized cementite particles were observed inside the ferrite grain.

(b) Sub-structure after Tensile Test

1. Lamellar Steel

Fig. 17 shows the dislocation structure when the samples were deformed by uniform extension. In between the cementite plates in this coarse lamellar steel, highly tangled dislocation structures were seen. It was difficult to obtain contrast of many dislocations in ferrite between the cementite plates in fine lamellar steels like LA, LB, LC, LD, because of possible very high dislocation density.

Fig. 18 shows well defined sub cell walls joining one fragmented cementite particle to another in a lamellar structure which was mainly composed of parallel cementite plates. The structure shown in Fig. 19 may be the intermediate stage between that of Fig. 17 and Fig. 18. The observation of no sub cell walls in ferrite between parallel cementite plates in Fig. 17 is consistent with the observation that in fine lamellar steels, the dislocation structure in the ferrite could not be resolved at all because of severe lattice strains due to high dislocation density.

2. Spheroidized Steel

Deformation by uniform extension of a fine spheroidized steel, SA produced a high dislocation density between cementite particles located at the grain boundaries (Fig. 20). A tendency to form sub cell walls could be recognized even in SA, but most dislocations were randomly distributed and well tangled. Near the cementite particles the dislocations were dense (Figs. 20 and 21). Sub cell walls can be seen in the ferrite grains. When much coarser spheroidized structures were deformed, well defined sub cell walls were observed, as shown in Fig. 22.

3. Armco Iron

No notable gradient of dislocation density from the grain boundary to the centre of the grain was observed in a polycrystalline material deformed

by uniform extension. However a disturbance of cell wall alignment near the grain boundary was recognizable, as seen in Figs. 23 and 24. At a region three microns away from the grain boundary, regular elongated sub cell walls were formed on planes parallel to $\{211\}$. The dislocation density within the sub grain is very low. In Fig. 24, some dislocations moving from the sub cell walls are seen.

5.2 Results of Tensile Test

(a) Presentation of Tensile Test Results

Typical experimental curves of load vs extension are shown in Fig. 25 for a lamellar steel, a spheroidized steel and an Armco iron. Logarithmic plots of true stress against true strain, with definitions

$$\sigma_{true} = \frac{L}{A_o} \cdot (e + 1) \tag{11}$$

$$\varepsilon = \ln (e + 1) \tag{12}$$

are given in Fig. 26, where e is the engineering strain; $(\frac{L}{A_o})$ the engineering stress, σ_{eng}; L the load; and A_o is the original cross sectional area. Values for the parameters k and n in the parabolic formula, $\sigma_{true} = k\ \varepsilon^n$ are given in Table 7. The pre-exponential constant k was found by extrapolating to $\varepsilon = 1.0$ in Fig. 26. All mechanical testing results are given in Tables 7 and 8.

(b) Stress-Strain Relation and the Parabolic Expression

It can be stated from Fig. 26 that for lamellar and spheroidized steels, the parabolic true stress-true strain relation is valid in a strain range from seven pct. to the strain where necking starts and for Armco iron, in a strain range from nine pct. to the strain where necking starts.

The work hardening coefficient, n was calculated by

$$n = \frac{(\log \sigma_{true}^{.10} - \log \sigma_{true}^{.075})}{(\log \varepsilon_{.10} - \log \varepsilon_{.075})}$$

where the subscripts stand for the strain range used. $\varepsilon_{direct}^{uniform}$ stands for the uniform extension determined directly from the load-extension curve as shown in Appendix III. $\varepsilon_{considere}^{uniform}$ was determined by drawing a tangential line from the measured σ_{true} - e curve to intercept the strain axis at -1.0, as shown in Appendix I. The maximum error in determination of $\varepsilon_{direct}^{uniform}$ was $\pm$ .005 for LC, $\pm$ .013 for SF and $\pm$ .022 for Armco A. The error limit in determination of $\varepsilon_{considere}^{uniform}$ was $\pm$ .01. The error limit in the determination of the pre-exponent constant, k was $\pm$ 20 x 10^3 psi for the lamellar steels and $\pm$ 5 x 10^3 psi for spheroidized steels and Armco iron.

The value of work hardening coefficient, n is plotted against $\varepsilon_{direct}^{uniform}$ and $\varepsilon_{considere}^{uniform}$ for each sample in Figs. 27A and 27B respectively. Figs. 27A and 27B indicate a linear relation between the n value and the uniform ductility. For a first approximation, it can be stated that uniform ductility is expressed by the work hardening coefficient in the present experiments.

(c) Dependence of Constants n and k on F.M.F.P.

Plots of the pre exponent constant, k, and the work hardening coefficient, n, against the F.M.F.P. of the undeformed structure are shown in Figs. 28 and 29 respectively. A straight line in the logarithmic plots implies a relation $k = A (\lambda_{ini})^a$ and $n = B (\lambda_{ini})^b$ where λ_{ini} = initial F.M.F.P. and Figs. 28 and 29 show that the larger the F.M.F.P., the larger is the work hardening coefficient, n, and the smaller is the pre-exponent constant, k.

An empirical relation between the work hardening coefficient and σ_{true}^{UTS} plotted in Fig. 30, shows that the smaller the work hardening coefficient

n, the larger is the σ_{true}^{UTS} . This may be due to the difference in dependence of k and n on the F. M. F. P.. From those figures, 28, 29 and 30, it can be concluded that the pre-exponent constant, k takes a dominant part at large strains, under the assumption of parabolic $\sigma_{true} - \varepsilon$ relation.

5.3 Results and Discussion of Void Observation

It was found that the technique proposed by Tanaka[75] et al was not suitable for void observation. The fracture at liquid nitrogen temperature produced too much plastic deformation. Figs. 31 and 32 show cleavage surfaces of lamellar and spheroidized steel respectively. This technique was abandoned. The direct sectioning technique as described previously was used.

(a) Lamellar Steel

Fig. 33 shows the structure of fine lamellar steel, LG on a section cut parallel to the tensile axis. The aligned black spots parallel to the tensile axis may be due to voids created during tensile deformation. An alignment of voids parallel to the tensile axis was predicted in McClintock's analysis for multiaxial stress cases[53]. He showed that when the nucleated voids were in high density they grew in a direction parallel to tensile axis. An alternate cause for the black spots are oxide inclusions. The aligned spots observed by these scanning microscopy observations (Fig. 33) were not thought to be oxide inclusions judging from their shape and contrast effect. Additional supporting evidence that the spots in Fig. 33 are not oxide inclusions is that nearby cementite plates are not disturbed by their existence. Puttick[62] has shown that cementite plates become irregular near oxide inclusions.

One rough estimate of the increase of volume due to voids or cracks formed was made on a lamellar steel. Even after being multiplied by a factor of three, the increment of volume was less than five pct. In this case oxides formed during etching were also counted because the volume of voids

was measured by using optical microscopy at a magnification of x1600.

(b) Spheroidized Steel

Fig. 34 is a scanning microscope picture taken from a coarse spheroidized steel. Some cementite particles were fractured leaving a void between the fractured surfaces. Fracture of cementite seems to take place at the narrowest region of a particle. This mode of fracture of cementite was most common. The fracture of the interface between particle and matrix was rarely observed.

(c) Armco Iron

Fig. 35A and 35B are for Armco B. One non-spherical cementite particle located at the grain boundary was fractured by shear. Between the fractured surfaces of this cementite particle, the matrix filled in, leaving no voids there. This is quite different from the case in spheroidized steel (Fig. 34). In spheroidized steel, the dislocation density is high resulting from a small grain size. To fill in the vacant region created by the fracture of the particle, less resistance for the dislocation motion, which carries the plastic strain in the deforming matrix, has to be present. In spheroidized steels, this might be difficult. On the other hand the barriers in Armco iron were not so high, and thus no void was left near the cementite particle. Fig. 34 also shows a crack formed between closely separated oxide inclusions. A relatively high local dislocation is expected here for the same reason described for spheroidized steel.

(d) Observation by Transmission Electron Microscopy

Fig. 36 was taken at the edge region of a thin foil from lamellar steel LG after the uniform extension. It shows clearly the steps formed in a cementite plate and is evidence for plastic deformation of cementite during room temperature deformation. It is not sure whether this is due to the

tensile deformation or the thin foil preparation. No detailed examination of this deformed cementite structure could be performed because it was seen at the edge of a thin foil which was bent from five to eight minutes of electron bombardment at a beam current of 10μ A. Fractured cementite plates and particles inside the thin foil were observed occasionally. Dislocation structures in the ferrite near the cracked cementite in lamellar and spheroidized steels could not be resolved, possibly due to severe lattice strain.

CHAPTER 6

DISCUSSION

6.1 Introduction

In the previous chapter on experimental results, it was revealed that the parabolic stress-strain relation was valid and uniform extension was linearly related to the work hardening coefficient, n. In Appendix I, theoretical arguments for the linear relation between the uniform extension and the work hardening coefficient are given. The following discussion will use these results to try to explain the effect of microstructure on the uniform ductility. To do this, the effect of microstructure is first formulated in terms of the Hall-Petch relation where the parameter of microstructure is the F.M.F.P., because the continuous and plastically deformable phase in the high carbon steel is ferrite. Based on this Hall-Petch equation, the uniform ductility was formulated as a function of reciprocal flow stress.

One attempt at a qualitative argument based on observations by electron microscopy is given.

6.2 Effect of Microstructure on the Strength of High Carbon Steels

(a) Dislocation Structures at Uniform Extension

As stated previously, the dislocation distribution in structures of coarse spheroidized steel (Figs. 21 and 22) and Armco iron (Figs. 23 and 24) was heterogeneous. In Armco iron, most of the dislocations were at sub cell walls. In spheroidized steel, they concentrated at either cell walls or near the cementite particles. It can be expected that a region where the

observed dislocation density is high may provide a large long range stress. In a region, where the observed dislocation density is low, the long range stress may also be low so that motion of dislocations is relatively free and strain can propagate. The latter region may provide stress relaxation for the former region. A mechanism of immobilization of dislocations, which is a kind of Cottrell locking, suggested by Evans and Rawlings[23] may be applicable for the build up of the long range stress.

Present observations imply that for sub cell walls to form, a critical spacing of initial ferrite may be required. Fine spheroidized and lamellar steels did not show sub cell walls. On the other hand, well defined sub cell walls were observed in the coarse spheroidized steel. However the dislocations are concentrated near the fragmented cementite particles (Figs. 18, 19 and 20), where the size of dislocation free regions is negligible. In fine spheroidized steel and lamellar steels, less relaxation of the local stress by dislocation motion is possible.

(b) Hall-Petch Relation

It was stated in the Literature Review that Ashby's one parameter work hardening theory[5] gave the Hall-Petch relation for two phase materials at small strains. To extend this for large strains, one has to include the experimental evidence that the wavelength of "statistically necessary dislocations" is reduced to the wavelength of geometrically necessary dislocations". This evidence is given in Keh's paper[42] on single crystal iron deformed at $0^{o}C$. This evidence adds complexity for theoretical analysis. According to the simplified Ashby's one parameter work hardening model, which neglects the behaviour of "statistically necessary dislocations", the Hall-Petch slope for cubic and plate-like second phase particles is given by equation (14)

$$k_{fl} = 2 \alpha G \sqrt{\varepsilon b A} \qquad (14)$$

and equation (6) gives

$$\sigma_{fl} = \sigma_i + 2\alpha G \sqrt{\varepsilon b} \cdot \frac{1}{\sqrt{\lambda_{ini}}} \qquad (15)$$

with $\gamma = 2\varepsilon$,

The flow stress at various strains listed in Table 8 is plotted in Fig. 37 against the initial F.M.F.P., $(\lambda_{ini})^{-1/2}$, listed in Tables 3 and 4. As is seen, for each type of microstructure, a linearity exists between the flow stress and $(\lambda_{ini})^{-1/2}$. The lamellar steel work hardens rapidly in the first few percent of strain. Above e = .075 both structures approximately satisfy the same Hall-Petch relation. Scatter in the data of spheroidized steels at large strains was much greater than that of lamellar steels, and evaluation of k_{fl} is less definite. Thus it is difficult to examine Ashby's theory predicting the increase of k_{fl} with increasing strain from the present results. Letting $\alpha = 1.5$[18, 25], $G = 7.9 \times 10^3$ kg mm^{-2} [2] and $b = 2 \times 10^{-7}$ mm the k_{fl}^{*} $_{e=.075}$ becomes 2.8 kg mm$^{-3/2}$. The observed Hall-Petch slope was k_{fl} $_{e=.075}$ = .50 kg mm$^{-3/2}$, (k_y = .55 kg mm$^{-3/2}$) in the present results, where the k_y is the Hall-Petch slope for the yield stress. In Fig. 38, the Hall-Petch plot is made using the sub cell diameter measured after the uniform extension. At least fifteen sub cells were measured in the thin foil. The Hall-Petch slope for this microstructural parameter was k_{fl} $_{e=.10}$ = .95 kg mm$^{-3/2}$, which is still lower than Ashby's prediction. Armstrong et al[2] obtained k_{fl} $_{e=.10}$ = 1.6 kg mm$^{-3/2}$ which was constant in a strain range from e = .05 to e = .20 (k_y = 2.2 kg mm$^{-3/2}$) for mild steels at room temperature. Liu[49] obtained k_{fl} $_{e=.10}$ = 2.0 kg mm$^{-3/2}$. Liu's experiments were on a wide variety of spheroidized steels (from c = .07 wt.% to 1.46 wt.%) with their F.M.F.P. determined by Fullman's technique, ranging from 3.8 μ to 18 μ . He was not concerned with the ferrite grain boundary which might be predominant in large F.M.F.P. materials.

---

* The numerical constant, A was tentatively taken as one.

Armstrong et al[27] pointed out that strain can introduce other processes, including sub cell wall formation, dislocation nucleation, and formation of obstacles to dislocations in a matrix covered by the initial F.M.F.P., λ_{ini}, which might decrease the k_{fl} effectively. These are all possible mechanisms in the present materials. No effort was given to analyze these factors in k_{fl}. For the following discussion, it is assumed that k_{fl} is constant with strain.

6.3 Effect of Microstructure on Uniform Ductility

(a) Introduction

The Hall-Petch slope, k_{fl} in Fig. 37 can be taken as constant with strain, and the change in frictional stress, σ_i, can be determined when the strain range is defined. The uniform ductility determined by Considere technique can then be predicted as a function of F.M.F.P., as follows.

A differentiation of the Hall-Petch equation (15)' gives equation (16)

$$\sigma_{fl} = \sigma_i + k_{fl} \cdot \frac{1}{\sqrt{\lambda_{ini}}} \qquad (15)'$$

$$\left(\frac{d\sigma_{fl}}{d\varepsilon}\right) = \frac{d\sigma_i}{d\varepsilon} + \frac{1}{\sqrt{\lambda}} \cdot \frac{dk_{fl}}{d\varepsilon} + k_{fl} \cdot \frac{d}{d\varepsilon}\left(\frac{1}{\sqrt{\lambda_{ini}}}\right) \qquad (16)$$

where the flow stress, σ is the true stress. From Fig. 37, $\frac{dk_{fl}}{d\varepsilon} = 0$, (which is not valid in Ashby's model) and $\frac{d}{d\varepsilon}\left(\frac{1}{\sqrt{\lambda_{ini}}}\right) = 0$ because λ_{ini} is the initial F.M.F.P., which is independent of plastic strain. Thus the equation (16) becomes

$$\left(\frac{d\sigma_{fl}}{d\varepsilon}\right) = \left(\frac{d\sigma_i}{d\varepsilon}\right) \qquad (17)$$

Appendix I gives

$$n = \frac{\varepsilon}{\sigma_{fl}} \cdot \left(\frac{d\sigma_i}{d\varepsilon}\right) \tag{18}$$

from (17) and (18),

$$n = \left(\frac{d\sigma_i}{d\varepsilon}\right) \cdot \varepsilon \cdot \frac{1}{\sigma_{fl}}$$

$$= A \cdot \frac{1}{\sigma_i + k_{fl} \frac{1}{\sqrt{\lambda_{ini}}}} \tag{19}$$

where $A = \left(\frac{d\sigma_i}{d\varepsilon}\right)$ which is independent of λ_{ini}. Thus the work hardening coefficient, n, becomes proportional to the reciprocal of flow stress and depends on the initial F. M. F. P., λ_{ini}, through the Hall-Petch relation. Appendix I and Figs. 27A, 27B give $n = \varepsilon^{uniform}$. In Fig. 39, the uniform ductility, $\varepsilon^{uniform}_{considere}$ is plotted against $(1/\sigma_{fl})$ at a given strain i. e. e = .075. A linear relationship exists between them. The work hardening coefficient, n for λ_{ini} = 4 microns can be found by taking $\frac{\Delta\sigma_i}{\Delta\varepsilon}$ = 153 kg mm^{-2} from the shift of Hall-Petch plot with the strain and σ_{fl} = 59.4 kg mm^{-2} (84 x 10^3 psi) at e = .075 corresponding to four microns of initial F. M. F. P. in Fig. 37. This gives n = .188. The corresponding uniform ductility, $\varepsilon^{uniform}_{considere} = .152 \pm .02$. The error of the estimate may be due to the evaluation of $\left(\frac{d\sigma_i}{d\varepsilon}\right)$.

Supporting evidence for the above argument is seen in Rosenfield and Hahn's paper[68]. They showed that the work hardening coefficient, n, was inversely proportional to the yield stress, σ_y as expressed by equation (7) of the Literature Review. In Fig. 40, σ_y is plotted against the flow stress at e = .10 for the present data. It is shown that there is a correlation between them. Gensemer's results[27, 7, 19] also agree with the present results.

(b) Physical Interpretation of the Present Observation

Plastic deformation at large strains includes two features i. e. plastic strain with work hardening, and the possible nucleation and growth of voids. If the plastic strain propagation by dislocations meets obstacles, either dynamic recovery or nucleation and growth of voids will take place. If the local stress concentration build up can be relaxed by propagating plastic strain (nucleation and movement of dislocations) or sub cell wall formation, as in the case of Fig. 35A and 35B, the voids will not be formed. If the former is difficult, then voids may be nucleated more readily as in the case of Fig. 34. This can be visualized in the most simple model expressed by

$$\gamma = b \cdot {}_{m} \cdot \lambda \qquad (20)$$

where r is the shear strain

λ is the distance dislocations move

${}_{m}$ is the mobile dislocation density

i. e. an absence of propagation of plastic strain is simply due to the absence of mobile dislocations available or/and absence of the space available for the dislocation movement.

Observation of voids which did not grow larger than the cementite particles in spheroidized steel (Fig. 34) shows the growth of voids is difficult. Observation of high dislocation densities, which were rather uniform throughout the lamellar and fine spheroidized steels, imply that stress concentrations could not be relaxed by plastic strain in a region of low dislocation density, or by dynamic recovery. Assume that voids existing at strain less than the uniform extension are very thin in the tensile direction. Since voids can not carry any load at all, for $\Delta p = O$ it may be valid to divide the decrement of the cross sectional area in equation (1), Appendix I into two parts, one due to external geometry dA and the other due to the existance of thin voids, dAv

$$\frac{dA}{A} + \frac{dA_v}{A} = \frac{d\sigma}{\sigma} \qquad (21)$$

Letting increment of strain $d\varepsilon_v = \frac{dA_v}{A}$,

$$\sigma = \frac{d\sigma}{d\varepsilon + d\varepsilon_v} \tag{22}$$

Equation (22) shows that a material in which many particles are fractured producing voids (as in Fig. 34) may have necking at a smaller strain and at a lower stress than one without voids. Thus voids formed during strain may govern the uniform extension.* Since at the onset of necking, all regions of the tensile sample are expected to be work hardened, one of the important factors determining the onset of necking may be the local dynamic recovery, as Cottrell[14] suggested, and the local density of voids.[33, 55, 63]

(c) Implications for Industrial Application

The yield strength, σ_y of spheroidized steel is as high as that of lamellar steel, as shown in Fig. 37. On the other hand, the spheroidized steel shows larger uniform extension as in Figs. 27A, 27B. Thus spheroidized steel in which the cementite particles are dispersed finely can satisfy industrial requirements for an application in structural members, plate steels, wire rope etc. for its high strength and has the advantage of a high ductility.

Research has begun to utilize the advantages of the high ductility and high strength of spheroidized steel on an industrial scale. Current developments of spheroidized steel are concerned with their production by thermo-mechanical treatments. Robbins et al[64] and Sherby et al[71] did experiments on hot (or warm) deformation to enhance the spheroidization and implied that the production of spheroidized steel can be done in a conventional steel works.

---

* Schematic representation of the argument is given in Fig. 41.

SUMMARY

Experimental data was used to formulate the effect of microstructure on the flow stress of high carbon steels. It was suggested that a better fit for the Hall-Petch equation was expected when using the sub cell diameter in the flow stress relationship.

The uniform ductility was formulated as a function of the reciprocal of flow stress, which is related to the microstructure through the Hall-Petch relation. The data agreed with this formulation. It was discussed relative to other published experimental formulations and agreed well. One attempt was given to interpret the formulation qualitatively using electron microscopic observations.

CHAPTER 7

SUGGESTION FOR FURTHER STUDIES

One important aspect which the present study avoided is the microscopic study on the behaviour of voids, which requires physically realistic theoretical models to be developed.

No attempt to estimate quantitatively the contributions of internal stress built by various dislocation structures observed in electron micrographs has been made.

This has to be solved by detailed examination of dislocation structures and their analysis into a simplified model, perhaps with the help of the computer.

For practical reasons, experimental data has to be accumulated for a wide range of microstructures.

APPENDIX I

In tensile loading of ductile materials, necking occurs when the maximum load corresponding to $\sigma_{eng.}^{U.T.S.}$ is reached. The plastic strain corresponding to $\sigma_{eng.}^{U.T.S.}$ is called uniform extension, $e^{uniform}$. Up to this strain, an increment of load, dp necessary to deform the sample further gradually decreases and at the onset of necking, dp = 0. The following equation is valid at this point.

$$dp = \sigma_{true}\, dA + A d\sigma_{true} = 0$$

from which $$\frac{-dA}{A} = \frac{d\sigma_{true}}{\sigma_{true}} \qquad (1)$$

when the volume of the deforming sample is kept constant,

$$dV = A d\ell + \ell\, dA = 0$$

from which $$\frac{dA}{A} = -\frac{d\ell}{\ell} = d\varepsilon \qquad (2)$$

where A: instantaneous cross sectional area and

ℓ: instantaneous gauge length

By combining (1) and (2)

$$\frac{d\sigma_{true}}{\sigma_{true}} = \frac{d\ell}{\ell} = d\varepsilon$$

from which

$$\frac{d\sigma_{true}}{d\varepsilon} = \sigma_{true} \qquad (3)$$

Assuming σ_{true} is related to, in the parabolic expression as

$$\sigma_{true} = k \varepsilon^{n} \tag{4}$$

The work hardening coefficient, n, is expressed by

$$n = \frac{d \ln \sigma_{true}}{d \ln \varepsilon} = \frac{d \sigma_{true}}{d \varepsilon} \quad \frac{\varepsilon^{uniform}}{\sigma_{true}}$$

From (3) and (5)

$$n = \varepsilon^{uniform} \tag{6}$$

From equation (3) above, another technique to determine the uniform extension can be established, termed considere technique[76]. The uniform extension is given at a tangental point on a σ_{true} - e curve obtained experimentally. The straight line, which is tangent, originates from the intercept - 1.0 on the e axis. By knowing ($d \ln \sigma_{true}/d \ln \varepsilon$) of the parabolic $\sigma_{true} - \varepsilon$ relation, the $\varepsilon^{uniform}$ is determined from equations (5) and (6).

In addition to these two techniques, there are three more techniques. These are:

1. intersection method[43, 51], which utilizes equation (3). Measure the work hardening rate, ($d \sigma_{true}/d\varepsilon$) at various strain and plot this against the ε. The $\varepsilon^{uniform}$ is where this curve intersects the $\sigma_{true} - \varepsilon$ curve.

2. plastic strain energy method[30], which requires a determination of the plastic strain energy covered by the $\sigma_{true} - \varepsilon$ curve when the parabolic stress-strain relation is valid.

3. direct reading method, which is to read the uniform extension from the recorded load-elongation chart when the elongation is measured by an accurate strain measuring device or to measure the gauge diameter away from the neck before and after the tensile test.

APPENDIX II

DETERMINATIONS OF F. M. F. P.

1. Spheroidized Steel

The symbols used are:

V_f: fraction of volume occupied by particles

λ_{ini}: F. M. F. P.; mean ferrite spacing terminated by spherical particles

λ: interparticle spacing, the spacing from the centers of a particle to that of a neighbouring particle

r: average radius of particles

N_v: number of particles per unit volume of the material

N_A: number of particles per unit area

N_L: number of particles per unit line length

L_{mat}: total length of ferrite matrix which is intercepted by a unit line length

Fullman[25] gave N_A and N_L for uniform size of spherical particles embedded in the matrix as:

$$N_A = 2r\, N_v \qquad (1)$$

$$N_L = \pi r^2\, N_v \qquad (2)$$

From (1) and (2)

$$r = \frac{2}{\pi} \cdot \frac{N_L}{N_A} \tag{3}$$

From the definition of the volume fraction, V_f, where V_f is equal to the product of particle volume, $4/3\ \pi r^3$ and N_v, combination of (2) and (3) with this gives

$$V_f = 4/3\ \pi r^3 \cdot N_v = \frac{8}{3\pi} \cdot \frac{N_L^2}{N_A} \tag{4}$$

Now, from the definition of L_{mat}, which is

$$L_{mat} = N_L\ \lambda_{ini} \tag{5}$$

and if the material is composed only of the spherical particles embedded in the matrix since the volume fraction, V_f is line fraction in this case

$$1 = (L_{mat} + V_f) = N_L \lambda_{ini} + V_f \tag{6}$$

from which

$$\lambda_{ini} = \frac{(1 - V_f)}{N_L} = \frac{3\pi N_A - 8 N_L^2}{3\ \pi\ N_A} \cdot \frac{1}{N_L} \tag{7}$$

2. Polycrystalline Iron

Let's assume the etched section of the polycrystalline iron shows composed of hexagonal shape for the ferrite grain which has constant size. The edge length, D and diameter, λ_{ini} of the hexagon are related to

$$D = \frac{1}{1.9} \cdot \lambda_{ini} \tag{1}$$

The area of a hexagon is $2.37D^2$ and the total area becomes equal to $2.37D^2 n_{At}$, where n_{At} is the total number of grains. Letting

$$n_A = \frac{n_{At}}{(\text{Area Observed})} \tag{2}$$

then

$$\lambda_{ini} = 1.25 \frac{1}{\sqrt{n_A}} \tag{3}$$

APPENDIX III

The load extension chart recorded by the Instron tensile machine gave a step like behavior. During work hardening, the load increased abruptly (20 - 40 lbs.) after a large extension at constant load. A schematic representation of the behavior is given in Fig. III-I. This may be due to character of the work hardened sample or Instron, i.e. mechanical sensitivity of recording pen responding to the signals in the recording unit. a/b in Fig. III-1 was 10 - 50 throughout the test. $a' \neq a$, on the otherhand, $b \simeq b'$. By extrapolating curves A and B of the regions before and after the onset of necking, the point of maximum load, P_{UTS} was found at point E. From these experimental observations $e^{uniform}_{direct}$, which was directly related to $\varepsilon^{uniform}_{direct}$, was determined. The strain between D; the midpoint of the highest stress region, and E was taken as the error limit, which is marked in Fig. 2-17(A).

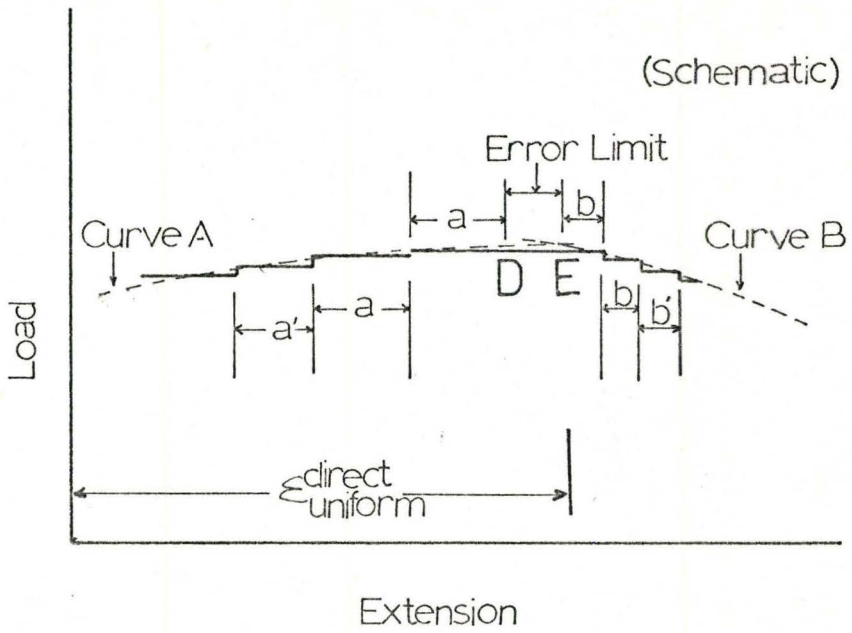

Fig. III-1: Schematic representation of load elongation chart near the maximum load.

REFERENCES

1. Airey, G. P., et al. (1968): The Growth of Cementite Particles in Ferrite. Trans. A.I.M.E., vol. 242, 1853.

2. Armstrong, R. et Al. (1962): The Plastic Deformation of Polycrystalline Aggregates. Phil. Mag. vol. 7, 45.

3. Armstrong, R. W. (1970): The Influence of Polycrystal Grain Size on Several Mechanical Properties of Materials. Met. Trans. A.I.M.E.-A.S.M., vol. 1, 1169.

4. Ashby, M. F. (1966): Work Hardening of Dispersion Hardened Crystals. Phil. Mag., vol. 14, 1157.

5. Ashby, M. F. (1970): The Deformation of Plastically Non-Homogeneous Materials. Phil. Mag., vol. 20, 399.

6. Barrett, C.S. and T.B. Massalski (1966): Structure in Carbon Steel and Decomposition of Austenite. Structure of Metals. McGraw-Hill, 513.

7. Blickwede, D. J. (1968): Sheet Steel - Micrometallurgy by Millions. Campbell Memo. Leci, Trans. A.S.M., vol. 61, 653.

8. Brammer, I.S. et al. (1966): Tables of Thin Film Techniques. Specimen Preparation for Electron Metallography. Blackwell Sci. Pub., Oxford, 67.

9. Brandon, D.G. and J. Nutting (1959): Technique for Preparing Thin Film of α-Iron. Brit. J. Appl. Phys., vol. 10, 255.

10. Brandon, D.G. and J. Nutting (1960): Dislocations in α-Irons. J.I.S.I., vol. 196, 160.

11. Bridgman, P. W. (1964): The Tension of Steel Under Pressure. Chap. 2. Studies in Large Plastic Flow and Fracture. Harvard Univ. Press, 71.

12. Brown, D. and N. Ridley (1966): Rate of Nucleation and Growth and Interlamellar Spacing of Pearlite in a Low Alloy Eutectoid Steel. J.I.S.I., vol. 204, 811.

13. Butcher, B.R. and H.R. Pettit (1966): Tensile Deformation and Cracking of Plane High Carbon Steels Containing Pearlite. J.I.S.I., vol. 204, 469.

14. Cottrell, A.H. (1963): Plastic Crystal, Chapt. 9, Mechanical Properties of Matters. John Wiley, 277.

15. Davidson, T.E. and G.S. Ansell (1969): Some Observations on the Relationship Between Effect of Pressure upon the Fracture Mechanisms and Ductility of Fe-C Materials. Trans. A.I.M.E. vol. 245, 2383.

16. De Hoff, R.T. (1968): Quantitative Microstructural Analysis. Fifty Years of Progress in Metallographic Techniques. Ed. and Publish.by A.S.T.M., 63.

17. Dieter, G.E. (1968): Introduction to Ductility. Chapt. 1 Ductility. Ed. by H.W. Haxton, A.S.M.

18. Dingley, D.J. and D. McLean (1967): Components of the Flow Stress of Iron. Acta. Met., vol. 15, 885.

19. Duckworth, W.E. and J.D. Baird (1969): Mild Steel. J.I.S.I., vol. 207, 854.

20. Edelson, B.I. and W.M. Baldwin Jr. (1962): The Effect of Second Phases on the Mechanical Properties of Alloys. Trans. A.S.M., vol. 55, 230.

21. Embury, J.D. and R.M. Fisher (1966): The Structure and Properties of Drawn Pearlite. Acta Met., vol. 14, 147.

22. Embury, J.D. et al. (1966): Substructural Strengthening in Materials Subject to Large Plastic Strains. Trans. A.I.M.E., vol. 236, 1252.

23. Evans, J.T. and R. Rawlings (1969): Work Hardening in Low Carbon Steel Deformed at Room Temperature. Mat. Sci. and Eng. vol. 4, 297.

24. Fisher, J.G. et al. (1953): The Hardening of Metal Crystals by Precipitate Particles. Acta Met. vol. 1, 336.

25. Fullman, R.L. (1953): Measurement of Particle Sizes in Opaque Bodies. Trans. A.I.M.E., vol. 197, 447.

26. Gensemer, M. et al. (1942): The Tensile Properties of Pearlite, Bainite and Spheroidite. Trans. A.S.M., vol. 30, 984.

27. Gensemer, M. (1946): Strength and Ductility. Trans. A.S.M., vol. 36, 30.

28. Gladman, T. et al. (1970): Work Hardening of Low Carbon Steels. J.I.S.I., vol 208, 172.

29. Gurland, J. and J. Plateau (1963): The Mechanism of Ductile Rupture of Metals containing Inclusions. Trans. A.S.M., vol. 56, 442.

30. Halford, G.R. (1963): The Strain Hardening Exponent - A New Interpretation and Definition. Trans. A.S.M., vol. 56, 787.

31. Ham, R.K. (1962): On the Loss of Dislocations During the Preparation of a Thin Film. Phil. Mag., vol. 7, 1177.

32. Holt, D.L. (1970): Dislocation Cell Formation in Metals. J. Appl. Phys., vol. 41, 3197.

33. Honeycombe, R.W.K. (1968): Fracture, Chapt. 15. Plastic Deformation of Metals. Edward Arnold, 453.

34. Honeycombe, R.W.K. (1968): The Deformation of Crystals Containing a Second Phase. Chap. 7. Plastic Deformation of Metals. Edward Arnold, 182.

35. Hull, F.C. and R.M. Mehl (1942): The Structure of Pearlite. Trans. A.S.M., vol. 30, 381.

36. Hume-Rothery, W. (1966): The System Iron-Carbon. Structure of Alloys of Irons. Pergamon Press, 139.

37. Hyam, E.D. and J. Nutting (1956): The Tempering of Plain Carbon Steels. J.I.S.I., vol.184, 148.

38. Ivanova, V.S. (1967): Role of Dislocations in Strengthening and Failure of Metals. Translated by J.E. Barker, N.P.L., Teddington.

39. Johnston, T. L. and C. E. Feltner (1970): Grain Size Effect in Strain Hardening Polycrystals. Met. Trans. A.I.M.E.-A.S.M., vol. 1, 1161.

40. Keh, A.S. and S. Weissman (1962): Deformation Sub Structure in Body Centered Cubic Metals. Electron Microscopy and Strength of Crystals. Ed. by Thomas and Washburn, Interscience Publ. 231.

41. Keh, A.S. (1963): Imperfections and Plastic Deformation of Cementite in Steel. Acta. Met., vol. 11, 1101.

42. Keh, A.S. (1965): Work Hardening and Deformation Sub-structure in Iron Single Crystals Performed in Tension at 298°K. Phil. Mag., vol. 12, 9.

43. Kelly, A. (1966): Dislocations. Strong Solids. Clarendon Press, Oxford, 63.

44. Kleemola, H.J. (1970): Strain Hardening Properties of .05%C and 1.0 Cu - 1.0 Ni - .05C Steels. J.I.S.I., vol. 208, 1025.

45. Langford, G. and M. Cohen (1969): Strain Hardening of Iron by Severe Plastic Deformation. Trans. A.S.M., vol. 62, 623.

46. Langford, G. (1970): A Study of the Deformation of Patented Steel Wire. Met. Trans. A.I.M.E.-A.S.M., vol. 1, 465.

47. Li, J.C.M. (1963): Petch Relation and Grain Boundary Sources. Trans. A.I.M.E., vol. 227, 239.

48. Li, J.C.M. and Y.T. Chou (1970): The Role of Dislocations in Flow Stress Grain Size Relationship. Met. Trans. A.I.M.E.-A.S.M., vol. 1145.

49. Liu, C.T. (1967): An Experimental Study of the Strengthening Mechanism and Fracture Behavior of Spheroidized Carbon Steels. Ph.D. Thesis, Brown University, 1967, U.S. Atomic Energy Commission Cont. No. A.T. (30-1) - 2394, Tech. Rep. No. 28.

50. Low Jr., J.R. (1968): Effect of Microstructure on Fracture Toughness of High Strength Alloys. Eng. Fract. Mechanics, vol. 1, 47.

51. Lubahn, J. D. (1946): The Necking of Tensile Test Specimens. Trans. A.S.M.E., vol. 68, 279.

52. Maurer, K. and D.H. Warrigton (1967): Deformation of Cementite. Phil. Mag., vol. 15, 321.

53. McClintock, F.A. (1968): A Criteria for Ductile Fracture by Growth of Hales. J. Appl. Mech., vol. 35, 363.

54. McGannon, H.E. (1964): Principles of Heat Treatment of Steel. Chap. 39, The Making, Shaping and Treating of Steel. U.S. Steel Corp., 1040.

55. McLean, D. (1962): Fracture. Mechanical Properties of Metals. John Wiley, 223.

56. McLean, D. (1962): Strain Hardening in Pure Metals. Mechanical Properties of Metals. John Wiley, 112.

57. Mogford, J.L. (1967): The Deformation and Fracture of Two Phase Materials. Met. Reviews. No. 114, vol. 12, 49.

58. Morrison, W.B. (1966): The Effect of Grain Size on the Stress-Strain Relationship in Low Carbon Steel. Trans. A.S.M. vol. 59, 824.

59. Palmer, G.I. et al. (1966): Some Aspects of Ductile Fracture in Metals. Physical Basis of Yielding and Fracture. By Inst. Phys and Phys. Soc. Conf. Series No. 1, Oxford, 53.

60. Palmer, G.I. and G.C. Smith (1968): Fracture of Internally Oxidized Copper - Alloys. Oxide Dispersion Strengthening. 2nd Bolton Landing Conf., N.Y. Ed. Ansell et al. Gordon and Breach, vol. 14, 253.

61. Pillissier, G.E. et al. (1942): Interlamellar Spacing in Pearlite. Trans. A.S.M., vol. 30, 1049.

62. Puttick, K.E. (1957): The Structure, Deformation and Fracture of Pearlite. J.I.S.I., vol. 185, 161.

63. Puttick, K.E. (1959): Ductile Fracture in Metals. Phil. Mag., vol. 4, 964.

64. Robbins, J.L. et al (1964): Accelerated Spheroidization of Eutectoid Steels by Concurrent Deformation. J.I.S.I., vol. 202, 804.

65. Roberts, C.S. et al. (1952): The Initiation of Plastic Strain in Plain Carbon Steels. Trans. A.S.M., vol. 44, 1150.

66. Rogers, H.C. (1960): The Tensile Fracture of Ductile Metals. Trans. A.I.M.E., vol. 218, 498.

67. Rogers, H.C. (1968): The Effect of Material Variables on Ductility. Ed. by Paxton, A.S.M., 31.

68. Rosenfield, A.R. and G.T. Hahn (1966). Numerical Descriptions of the Ambient, Low Temperature and High Strain Rate Flow and Fracture Behavior of Plain Carbon Steel. Trans. A.S.M., vol. 59, 962.

69. Rosenfield, A.R. (1968): Criteria for Ductile Fracture of Two Phase Alloys. Met. Reviews No. 121, 29.

70. Rostoker, W. and J.R. Dvorak (1965): Quantitative Metallography. Chapt. 5. Interpretation of Metallographic Structures. Academic Press, 195.

71. Schankula, M.H. et al. (1970): The Accumulation of Dislocations During the Deformation of Polycrystals. Acta. Met., vol. 18, 1293.

72. Sherby, D. et al. (1969): Development of Fine Spheroidized Structures by Warm Rolling of High Carbon Steels. Trans. A.S.M, vol. 62, 575.

73. Smith, C.S. (1948): Grain Phases, and Interfaces: An Interpretation of Microstructure. Trans. A.I.M.E., vol. 175, 15.

74. Sundquist, B.E. (1968): The Edgewise Growth of Pearlite. Acta. Met., vol. 16, 1413.

75. Tanaka, K. et al. (1970): Cavity Formation at the Interface of a Spherical Inclusions in a Plastically Deformed Matrix. Phil. Mag., vol. 21, 267.

76. Tegart, W.J. McG. (1966): Stress-Strain Relationship in Static and Dynamic Tension. Elements of Mechanical Metallurgy, MacMillan, 17.

77. Turkalo, A.M. and J.R. Low, Jr. (1958): The Effect of Carbide Dispersion on the Strength of Tempered Martensite. Trans. A.I.M.E., vol. 212, 750.

78. Wilson, D.V. and Y.A. Konnan (1964): Work Hardening in a Steel Containing a Coarse Dispersion of Cementite Particles. Acta. Met., vol. 12, 617.

Table 1: Chemical Composition of As-received Materials

Chemical Composition of
As-received Materials

wt.%

	Tensile Sample	C	Mn	S	Si	Ni	Cr
Group 1	LB LC LD LE LG SB SC SE SF	.830	.45	.044	.244	Nil.	Nil.
Group 2	LA LF SA SD	.947	.45	.054	.265	Nil.	Nil.

Nil. = Less than .025

Table 2: Carbon Content after Heat Treatment

Carbon Content after
Heat Treatment

wt.%

	LA	LB	LC	LD	LE	LF	LG
C	.928	.786	.785	.776	.805	.881	.794

	SA	SB	SC	SD	SE	SF
C	.950	.902	.758	.901	.770	.681

Table 3: Interlamellar Spacing and F. M. F. P. for Lamellar Steels

	microns			microns		
	Int Lam Spacing			Initial F.M.F.P.		
	av.	min.	max.	av.	min.	max.
LA	.14	.12	.16	.10	.08	.12
LB	.15	.13	.16	.11	.09	.12
LC	.20	.18	.22	.16	.14	.18
LD	.30	.26	.38	.24	.20	.32
LE	.28	.23	.30	.22	.17	.24
LF	.30	.24	.36	.24	.18	.30
LG	.52	.44	.65	.42	.34	.55

Table 4: F. M. F. P. and Other Microstructural Parameters for Spheroidized Steels

	microns						microns		
	Radius of Particles			Volume Fraction			Initial F.M.F.P.		
	av.	min.	max.	av.	min.	max.	av.	min.	max.
SA	.70	.66	.75	.55	.45	.72	.79	.65	1.1
SB	.68	.40	.80	.49	.29	.60	2.5	2.0	2.6
SC	.81	.72	.96	.35	.44	.72	2.6	2.4	2.9
SD	.82	.66	.95	.32	.23	.44	2.5	1.6	3.1
SE	1.2	1.0	1.4	.29	.22	.43	6.3	5.4	7.1
SF	1.2	.90	1.4	.31	.22	.42	6.3	5.6	7.4

Table 5: Ferrite Grain Size in Spheroidized Steels by Smith's Model

microns

	Grain Diameter		
	av.	min.	max.
SA	1.8	1.5	2.3
SB	1.8	1.2	3.0
SC	2.1	1.8	2.1
SD	3.0	2.8	4.1
SE	5.9	4.5	7.0
SF	5.4	3.9	6.9

microns

	Grain Diameter		
	av.	min.	max.
Armco A	35.	31.	38.
Armco B	29.	-	-

Table 6: Ferrite Grain Size in Armco Iron

Table 7: Results of Mechanical Testing, 1.

		uniform ductility			10^3 PSI pre-exp. const	10^3 PSI
		$\varepsilon_{uniform\ considere}$	$\varepsilon_{uniform\ direct}$	n value	K	$\sigma_{UTS\ true}$
LA	1		.054			144.5
	2		.053			152.2
	3		.052			140.0
	av.		.053			145.6
LB	1	.090	.095	.096	244.	169.8
	2	.100	.103	.118	200.	148.4
	3	.081				
	av.	.090	.099	.107	222.	159.1
LC	1	.095	.100	.107	203.	143.7
	2	.095	.103	.100	190	140.1
	3	.109	.140	.114	175.	143.9
	av.	.100	.114	.104	189.	142.9
LD	1	.095		.128	215.	
	2	.122	.103	.153	194.	131.2
	3	.095	.093	.124	205.	130.5
	av.	.104	.098	.135	205.	130.9
LE	1	.104	.098	.181	198.	128.0
	2	.104	.093	.114	183.	128.7
	3	.100	.116	.168	175.	130.5
	av.	.103	.102	.154	185.	129.1
LF	1	.109	.118	.137	200.	134.7
	2	.109	.118	.144	202.	134.9
	3	.109	.120	.144	190.	135.8
	av.	.109	.119	.142	198.	135.1
LG	1	.135	.120	.181	172.	112.3
	2	.118	.120	.169	167.	114.3
	3	.128	.120	.162	163.	114.8
	av.	.127	.120	.171	167.	113.8

Table 7 - Cont'd.

		uniform ductility			pre exp		10^3 PSI
		$\varepsilon_{uniform\ considere}$	$\varepsilon_{uniform\ direct}$	n value	K const.		$\sigma_{UTS\ true}$
SA	1	.118	.134	.139	149.		111.9
	2	.113	.116	.142	154.		110.8
	3	.118	.131	.130	138.		109.6
	av.	.116	.127	.137	147.		110.8
SB	1	.140					
	2	.140	.166	.147	150.		119.5
	3	.127	.133	.154	142.		110.1
	av.	.136	.150	.151	146.		112.3
SC	1	.153	.174	.172	147.		105.5
	2	.153	.164	.177	146.		104.6
	3	.153	.168	.175	142.		106.4
	av.	.153	.169	.175	145.		105.5
SD	1	.131	.135	.157	137.		95.2
	2	.131	.148	.187	138.		95.8
	3	.127	.142	.177	129.		94.9
	av.	.130	.142	.174	135.		95.6
SE	1	.165	.203	.207	138.		112.0
	2	.170	.201	.192	139.		106.4
	3	.165	.189	.191	140.		105.4
	av.	.165	.198	.200	139.		107.6
SF	1	.170	.199	.235	126.		91.3
	2	.170	.191	.209	125.		92.3
	3	.165	.178	.220	128.		93.1
	av.	.168	.189	.221	126.		92.2
Armco A	1	.227		.322	80.3		
	2	.237	.265	.291	75.0		51.8
	3	.207	.245	.300	74.0		50.5
	av.	.223	.256	.304	76.3		51.2
Armco B	1	.235	.262	.294	80.0		53.6
	2	.251	.281	.272	78.0		54.3
	3	.235	.310	.316	82.0		56.6
	av.	.239	.284	.295	80.0		54.8

Table 8: Results of Mechanical Testing, 2 - Flow stress at various strains

10^3 PSI

		σ_{true}^{LYP}	$\sigma_{true}^{e=.075}$	$\sigma_{true}^{e=.10}$	$\sigma_{true}^{e=.125}$
LA	1	70.0			
	2	71.3			
	3	74.1			
	av.	71.3			
LB	1	74.6	165.2	169.7	
	2	61.6	142.5	147.3	
	3				
	av.	68.1	153.9	158.5	
LC	1	55.9	138.2	143.1	
	2	58.9	135.3	139.1	
	3	62.5	137.2	141.1	
	av.	59.1	136.9	141.3	
LD	1	57.6	129.1	133.7	
	2	57.1	124.9	132.3	
	3	58.0	126.2	130.7	
	av.	57.6	126.7	131.6	
LE	1	49.7	123.5	127.8	
	2	47.5	125.1	129.0	
	3	48.5	125.3	128.1	
	av.	48.6	124.6	128.3	
LF	1	53.7	126.3	131.2	134.3
	2	53.8	126.8	131.9	135.1
	3	51.9	126.4	131.5	135.0
	av.	53.1	126.5	131.5	134.8
LG	1	25.1	103.7	109.0	113.4
	2	23.5	105.7	110.5	113.9
	3	29.5	106.3	111.1	114.6
	av.	26.0	105.1	110.2	113.6

Table 8 - Cont'd.

10^3 PSI

		σ_{true}^{LYP}	$\sigma_{true}^{e=.075}$	$\sigma_{true}^{e=.10}$	$\sigma_{true}^{e=.125}$	$\sigma_{true}^{e=.15}$	$\sigma_{true}^{e=.20}$	$\sigma_{true}^{e=.25}$
SA	1	74.9	102.8	106.8	110.2			
	2	67.7	97.1	48.6				
	3	74.1	102.0	105.7	108.1			
	av.	72.3	100.5	103.6	109.5			
SB	1	78.6	100.7	106.1	110.0	113.2		
	2	78.5	101.3	105.5	109.8	111.5		
	3	78.1	100.6	105.0	108.1			
	av.	78.4	100.9	105.5	109.8	112.4		
SC	1	63.3	91.4	95.8	99.2	102.3		
	2	63.2	90.5	95.1	98.4	101.4		
	3	64.9	92.1	96.5	100.5	103.1		
	av.	63.8	91.3	95.9	99.4	102.3		
SD	1	62.6	86.5	90.4	93.5			
	2	61.9	85.2	89.8	92.9	95.0		
	3	60.0	84.9	89.2	92.4	94.7	100.7	
	av.	61.5	85.5	89.8	92.9	94.9		
SE	1	59.8	84.5	89.6	93.1	96.1		
	2	62.5	88.6	93.4	96.7	99.6	104.4	
	3	58.0	88.9	93.7	97.1	100.4	104.7	
	av.	58.8	87.3	92.2	95.6	98.7		
SF	1	49.5	74.4	79.4	83.0	85.8		
	2	49.9	76.4	81.0	84.4	87.3		
	3	52.1	78.0	82.9	86.4	89.0		
	av.	50.5	76.3	81.1	84.6	87.4		
Armcol A	1	21.4	35.6	39.0	41.7	43.8	47.3	49.9
	2	16.5	35.3	38.8	41.3	43.6	46.8	49.5
	3		35.7	39.3	41.9	44.0	47.2	
	av.	19.0	35.5	39.0	41.6	43.8	47.1	49.7
Armcol B	1	16.7	36.5	40.3	42.9	45.3	48.7	51.3
	2	12.0	37.4	40.2	42.7	44.9	48.6	51.1
	3	17.3	36.9	40.5	43.3	45.6	49.0	51.7
	av.	17.0	36.9	40.3	43.0	45.3	48.6	51.4

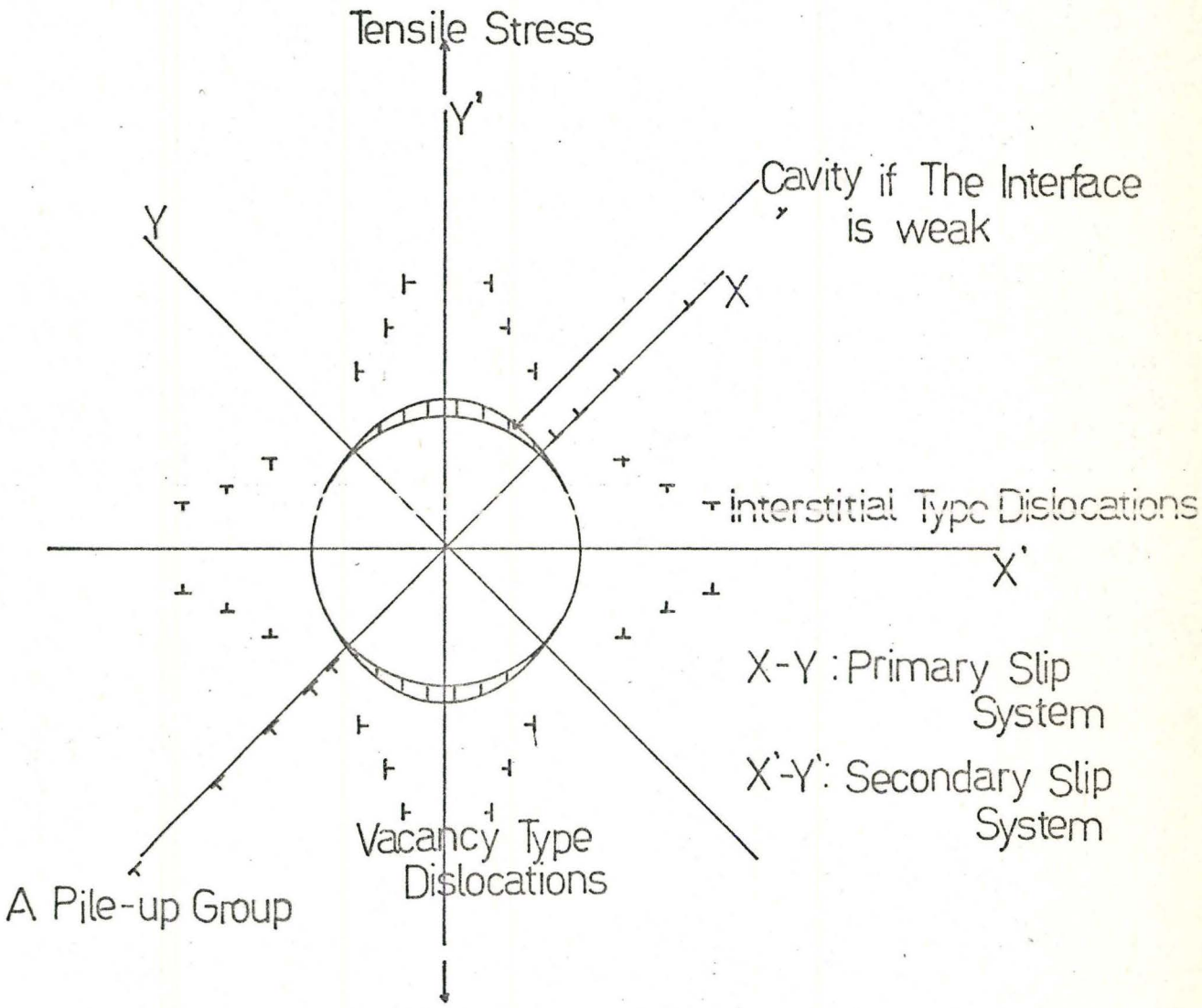

Fig. 1: Schematic representation of Ashby's Void Initiation Model

Fig. 2: Heat Treatment Cycles

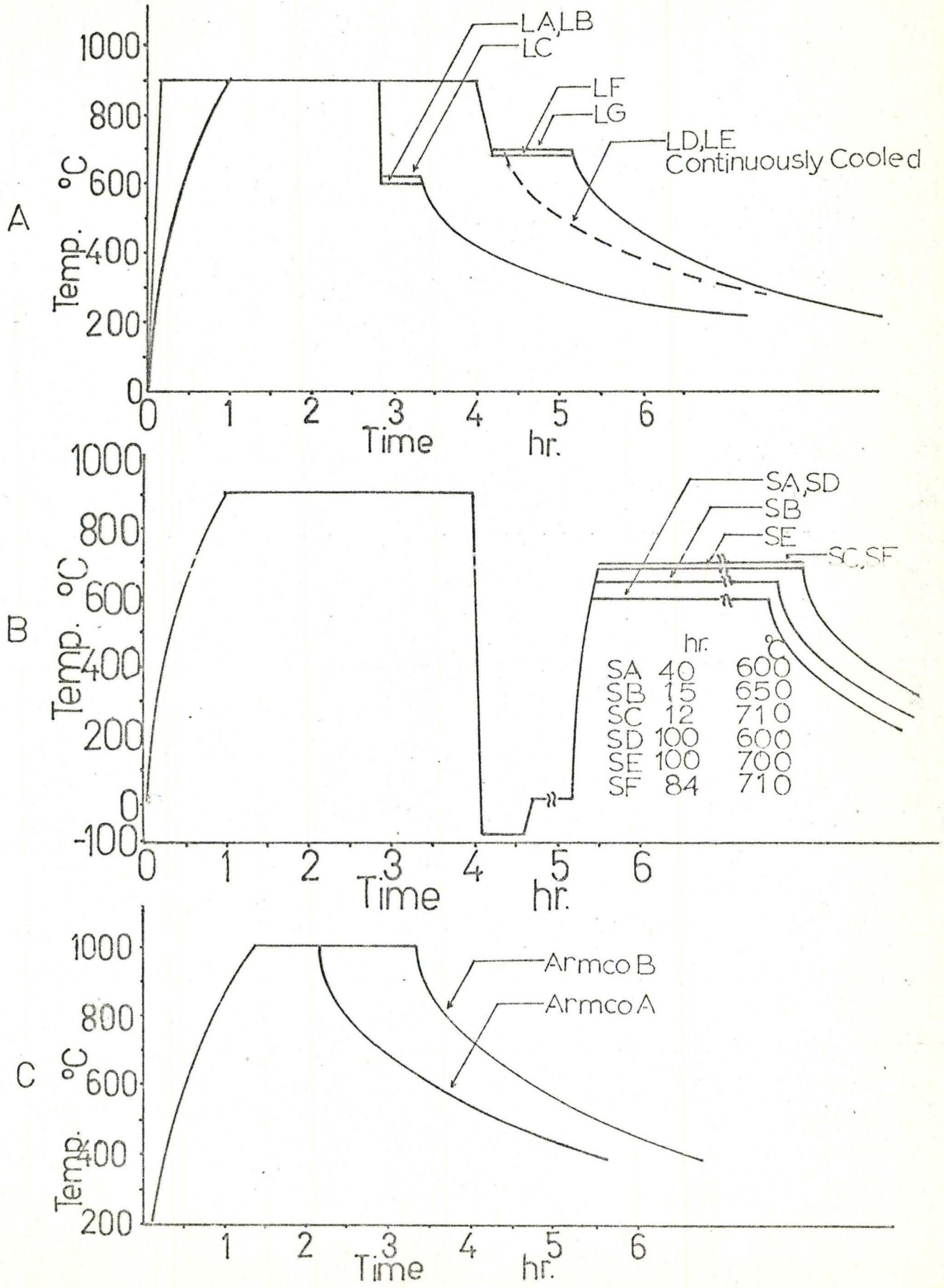

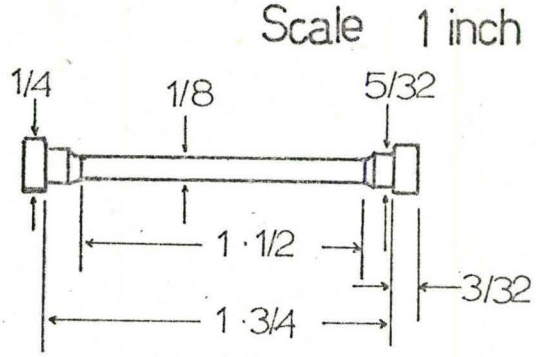

Fig. 3: Tensile Test Sample

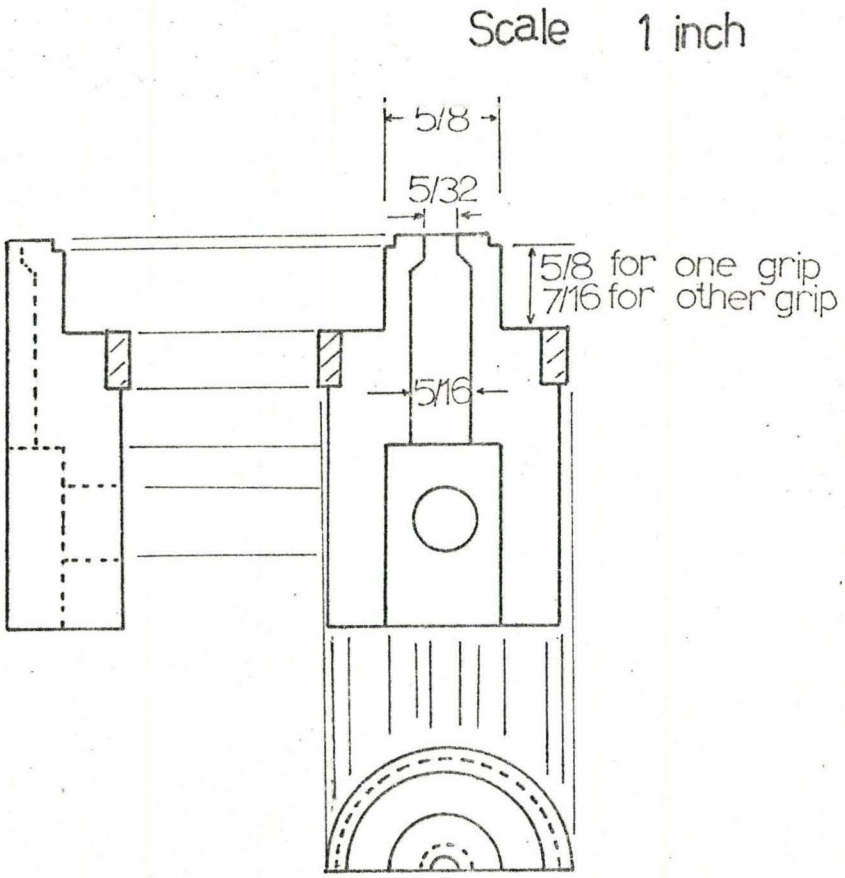

Fig. 4: Design of Grip System

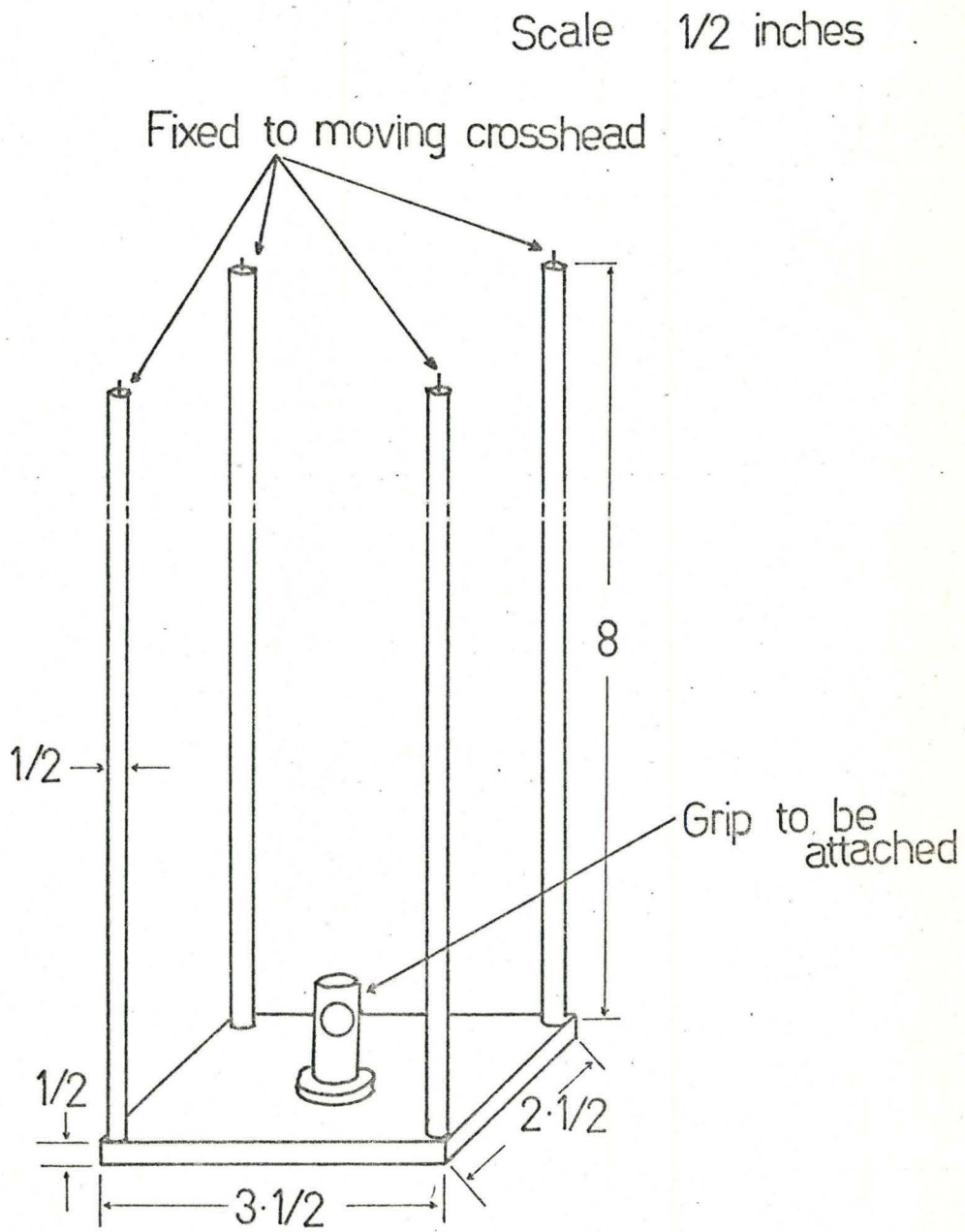

Fig. 5: Design of Cross Head Fixture.

Fig. 6: Schematic representation of applied voltage and current density.

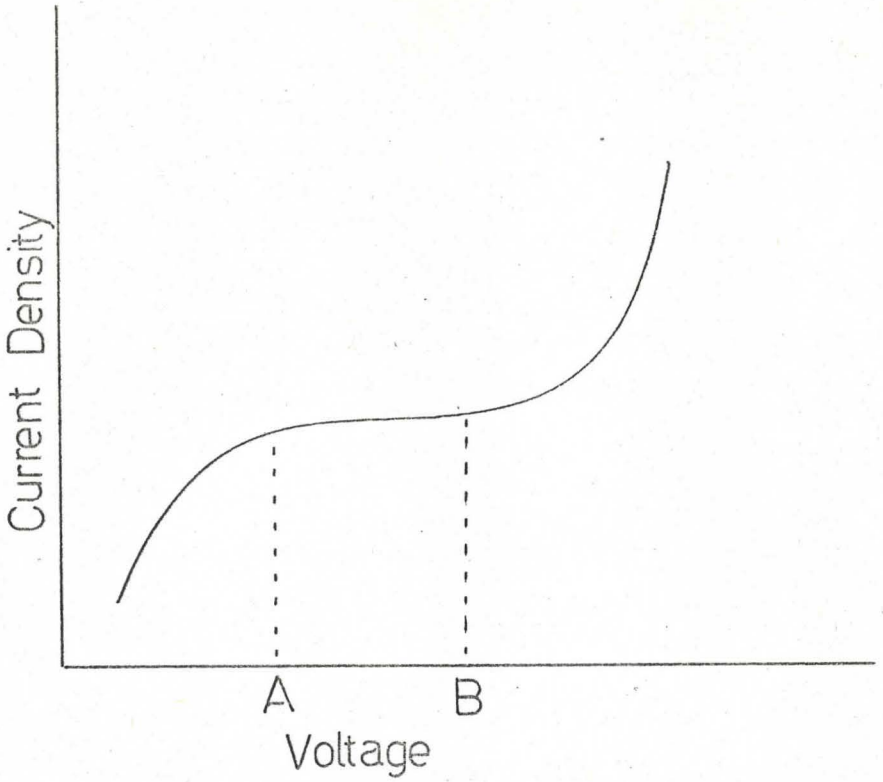

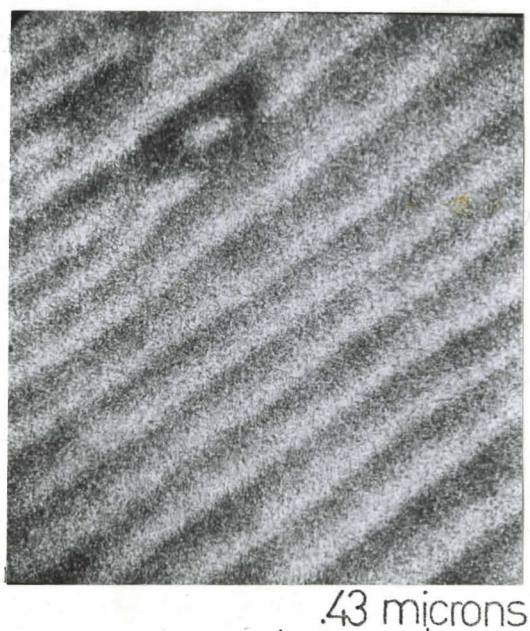

LA, Longitudinal section to tensile axis

Fig. 7: Highly magnified scanning electron micrograph of lamellar steel before the test.

LG, Longitudinal section to tensile axis

Fig. 9: A typical transmission electron micrograph of lamellar steel before the test.

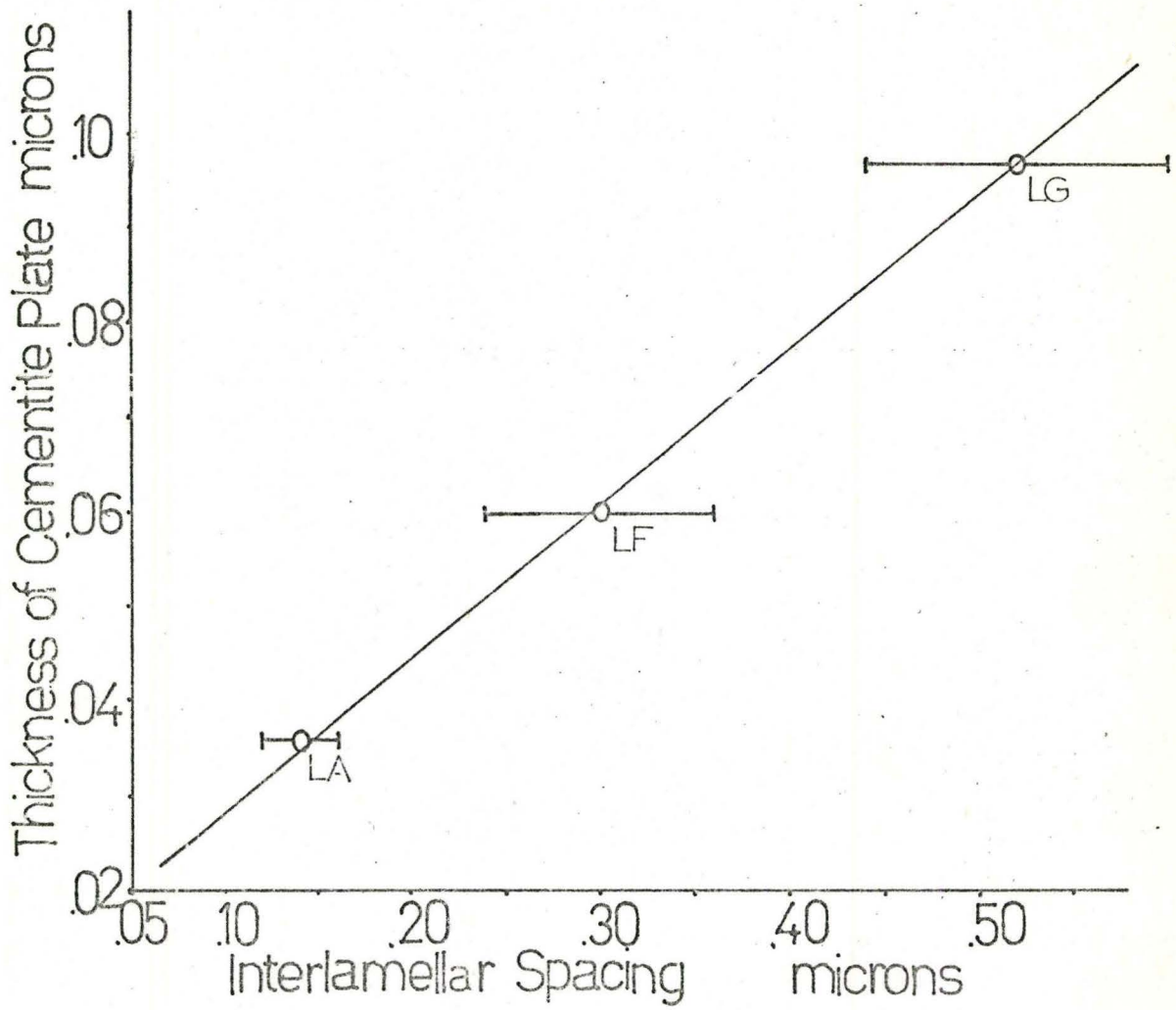

Fig. 8: Dependence of thickness of cementite plate on interlamellar spacing.

Fig. 10: A typical optical micrograph of spheroidized steel before the test.

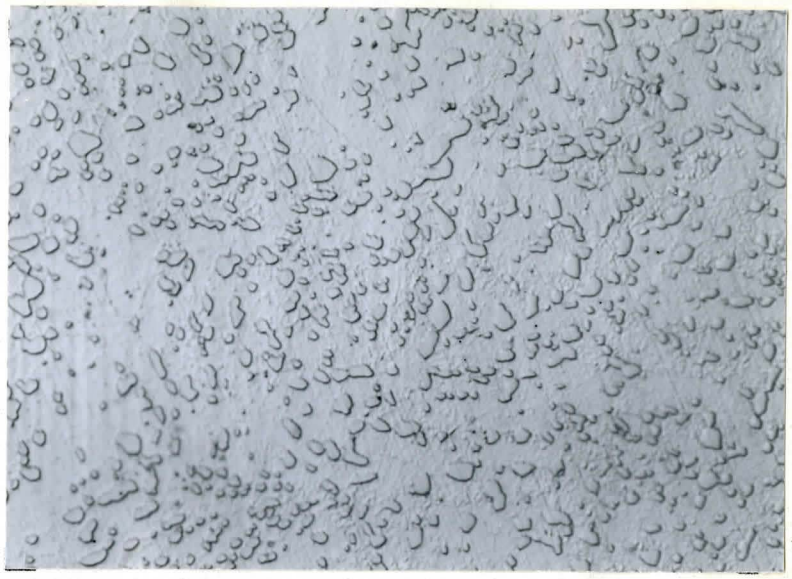

SF

20. microns

Fig. 11: A typical optical micrograph of Armco iron before the test.

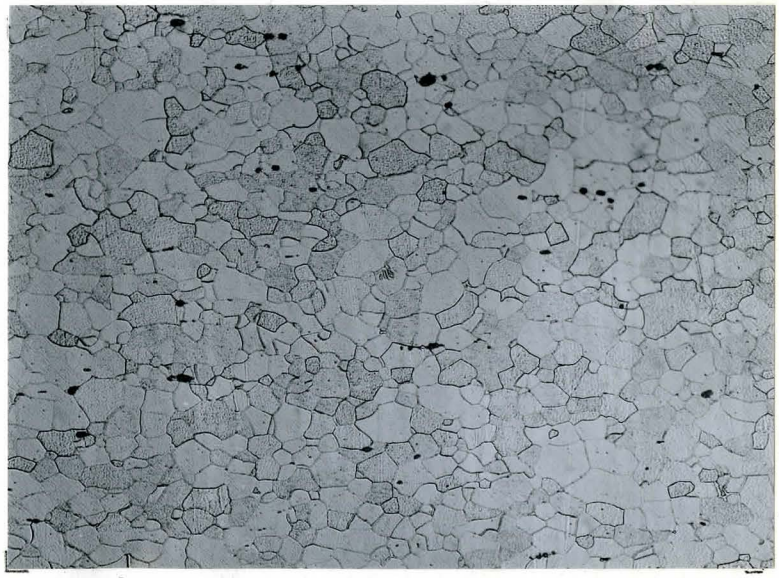

A

Armco A
200. microns

B

Armco B
200. microns

5.0 microns

LE, Longitudinal

Fig. 12: Transmission electron micrograph of lamellar steel showing a grain boundary running across the lamellar structure.

1.4 microns

LF, Longitudinal

Fig. 13: A typical transmission electron micrograph of lamellar steel showing no sub cell walls in the ferrite before the test.

5.0 microns

SF, Longitudinal

Fig. 14: Substructure of spheroidized steel showing no sub cell walls or dislocations in ferrite grains before the test.

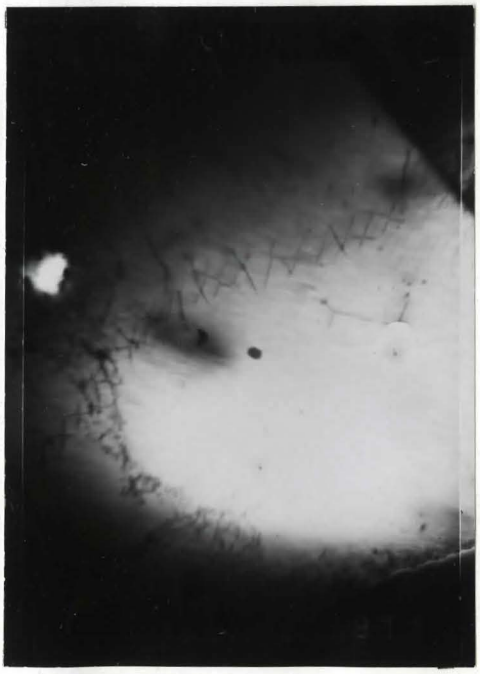

5.7 microns

Armco B, Longitudinal

Fig. 16: Sub cell walls running from the high angle boundary in Armco iron before the test.

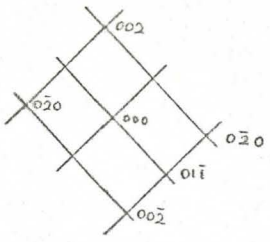

Zone Axis = 100

A

Assuming that the beam is parallel to the zone axis in Figs. 15A and 15B, the resultant misfit angle at the boundary becomes 63.4°.

B

SB Long.

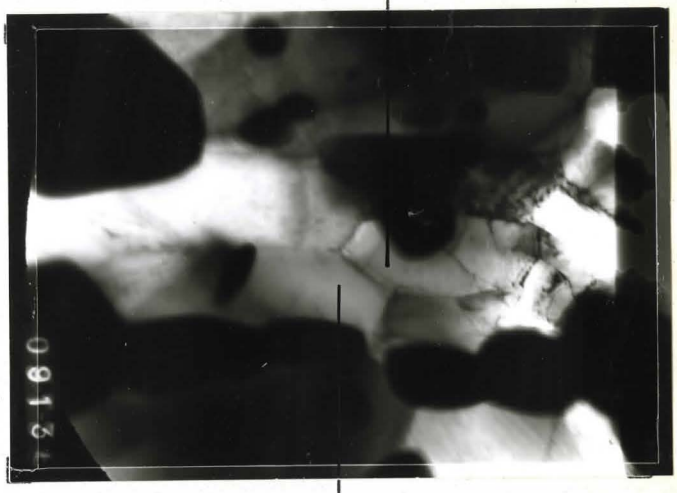

1.1 microns

C

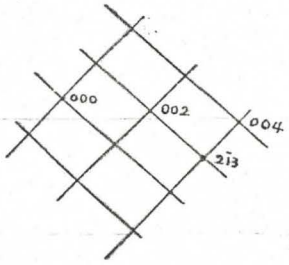

Zone Axis = 120

Fig. 15: Misorientation at a ferrite boundary in a spheroidized steel before the test.

.42 microns

LG, Transverse

Fig. 17: Tangled dislocations between the cementite plates of lamellar steel with no sub cell wall.

LG, Transverse

Fig. 18: High dislocation density near the fragmented cementite subdividing the matrix observed in a coarse lamellar steel.

.71 microns

LG, Transverse

Fig. 19: Dislocation structure at the tips of discontinuous cementite plates.

.67 microns

SA, Transverse

Fig. 20: Extensive tangled dislocation structures with less clearly defined sub cell walls observed in a finely dispersed spheroidized steel.

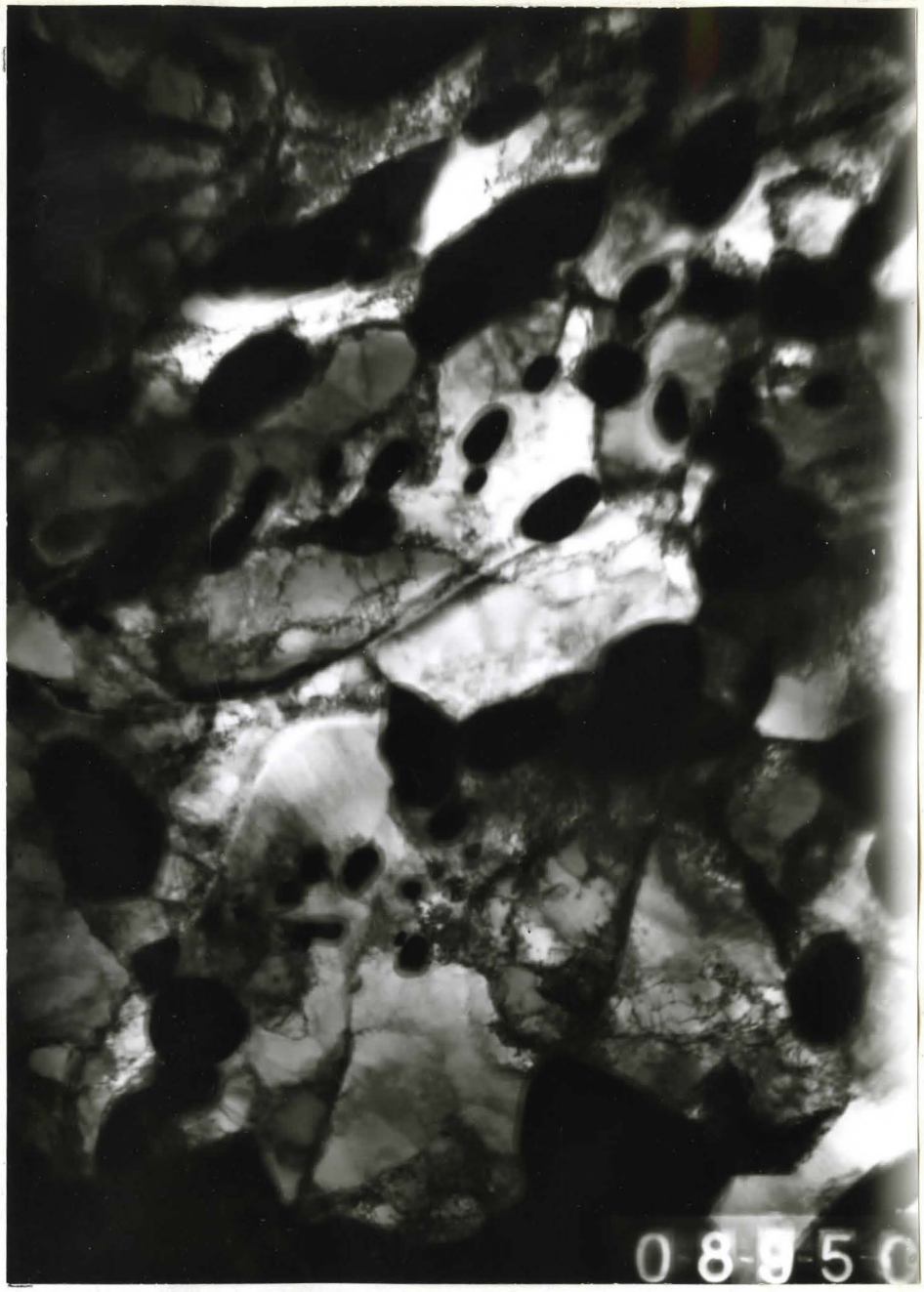

1.2 microns

SB, Transverse

Fig. 21: Accumulation of dislocations near the cementite particles.

.42 microns

SF, Longitudinal

Fig. 22: Well defined cell walls seen in a coarsely dispersed spheroidized steel.

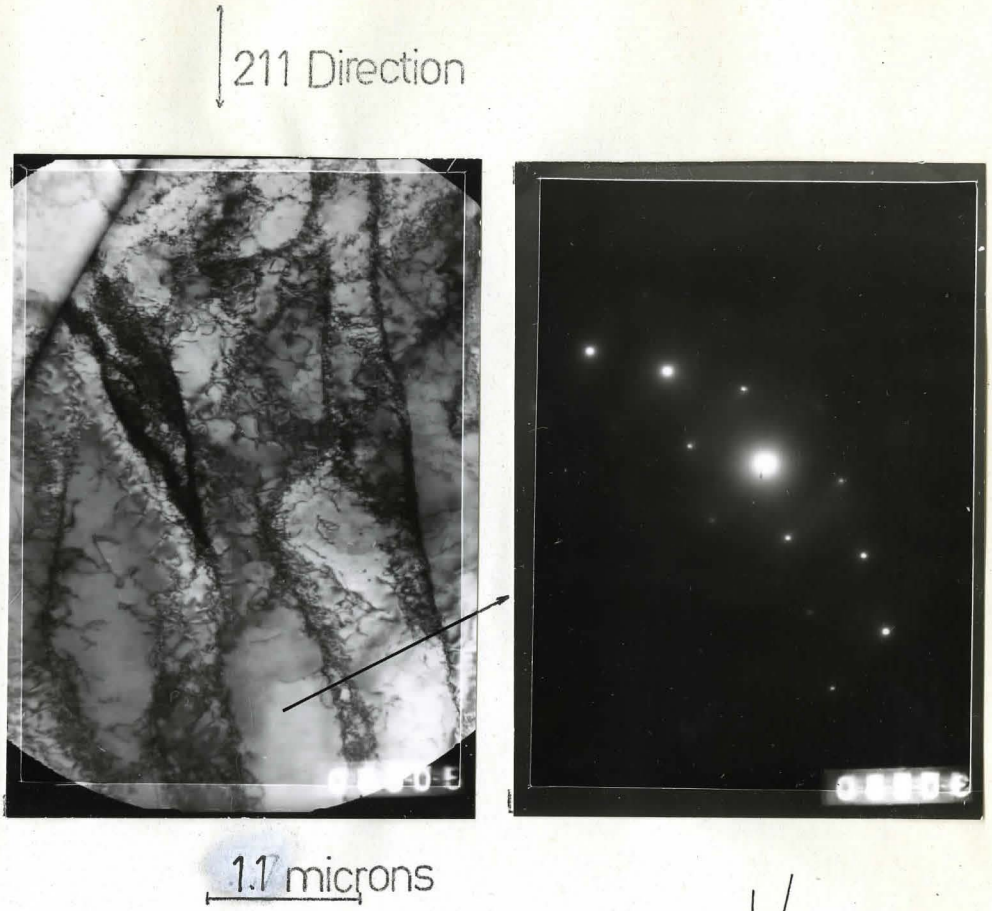

Armco A, Longitudinal

Direction A in the electron micrograph corresponds to direction B in the S. A. D.. The calibrated rotation angle for this magnification is 9°.

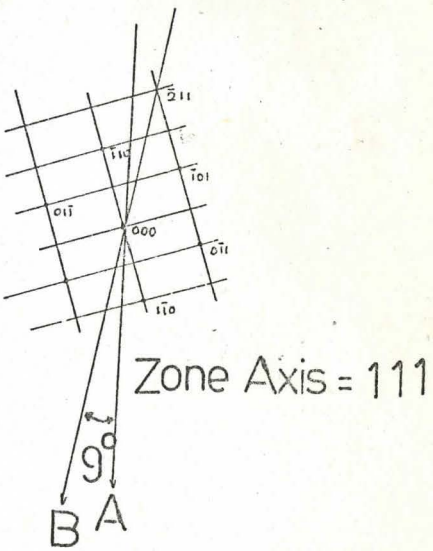

Fig. 23: Well defined cell walls near the high angle boundary.

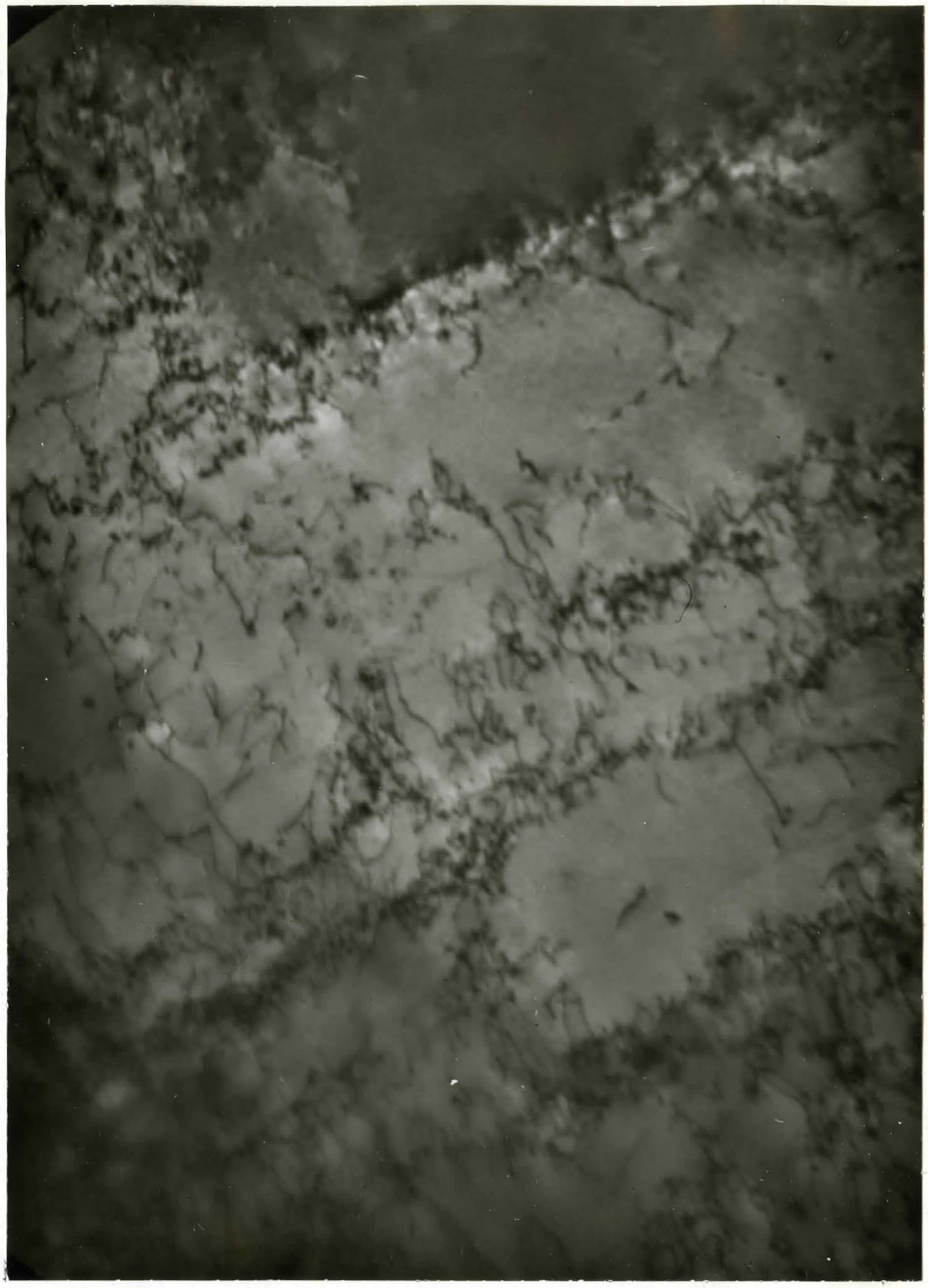

.57 microns

Armco A, Longitudinal

Fig. 24: Well defined parallel cell walls observed in Armco iron.

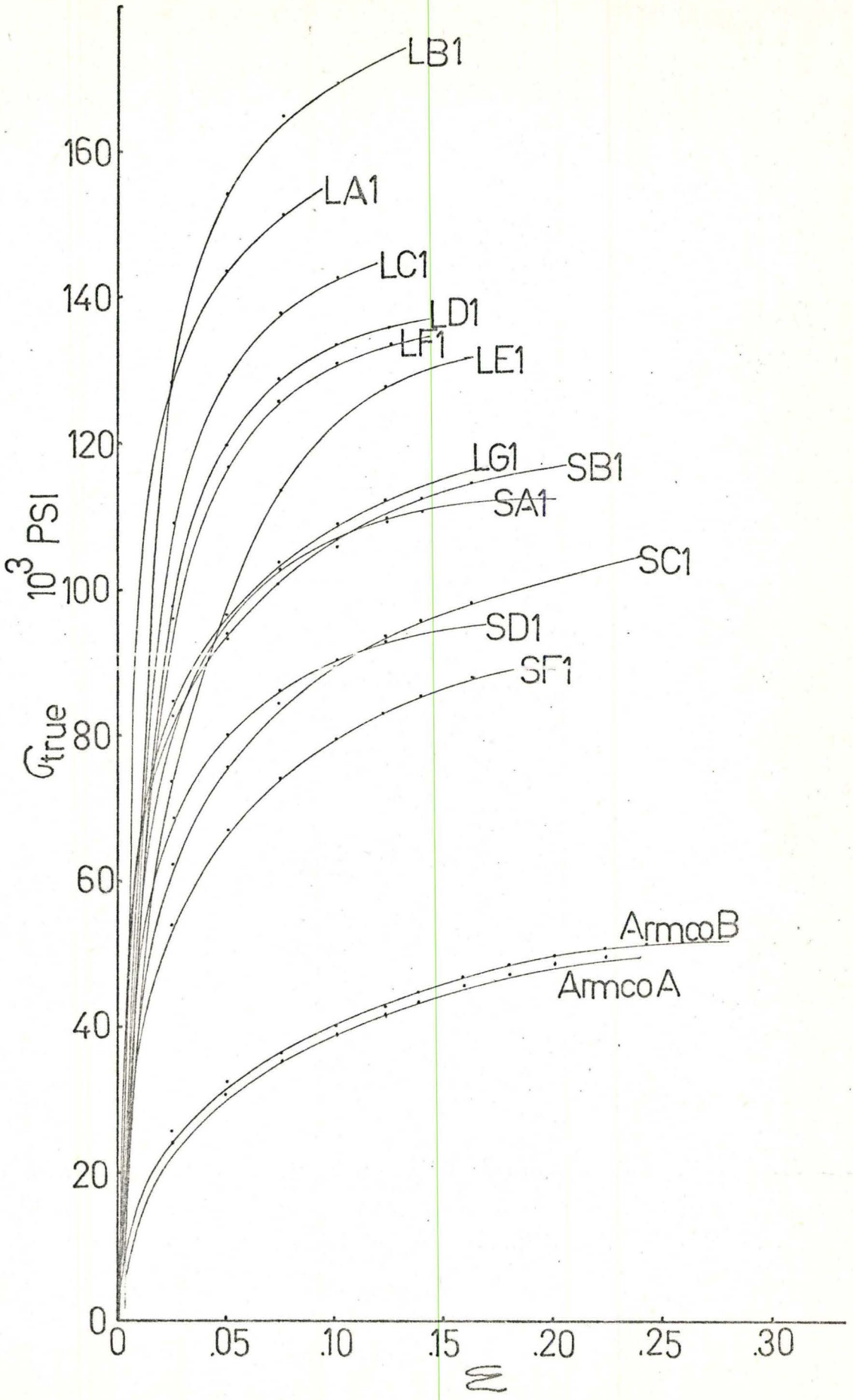
LB1
LA1
LC1
LD1
LF1
LE1
LG1
SB1
SA1
SC1
SD1
SF1
Armco B
Armco A
160
140
120
100
80
60
40
20
0
10^3 PSI
σ_{true}
0
.05
.10
.15
.20
.25
.30
ε

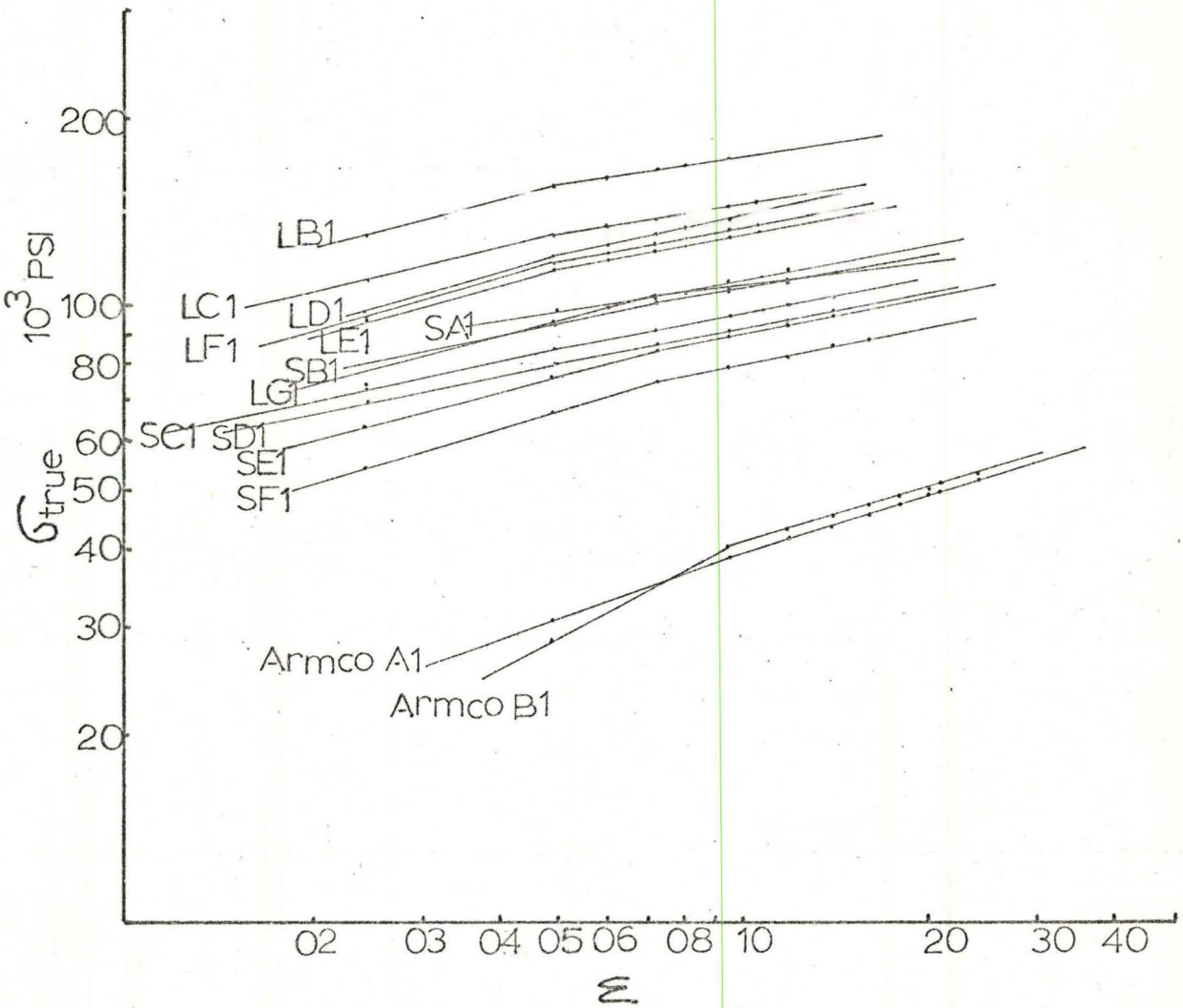

Fig. 26: Logarithmic true stress-true strain curves showing a linearity at strains over $\varepsilon = .075$ for lamellar and spheroidized steels and $\varepsilon = .09$ for Armco iron.

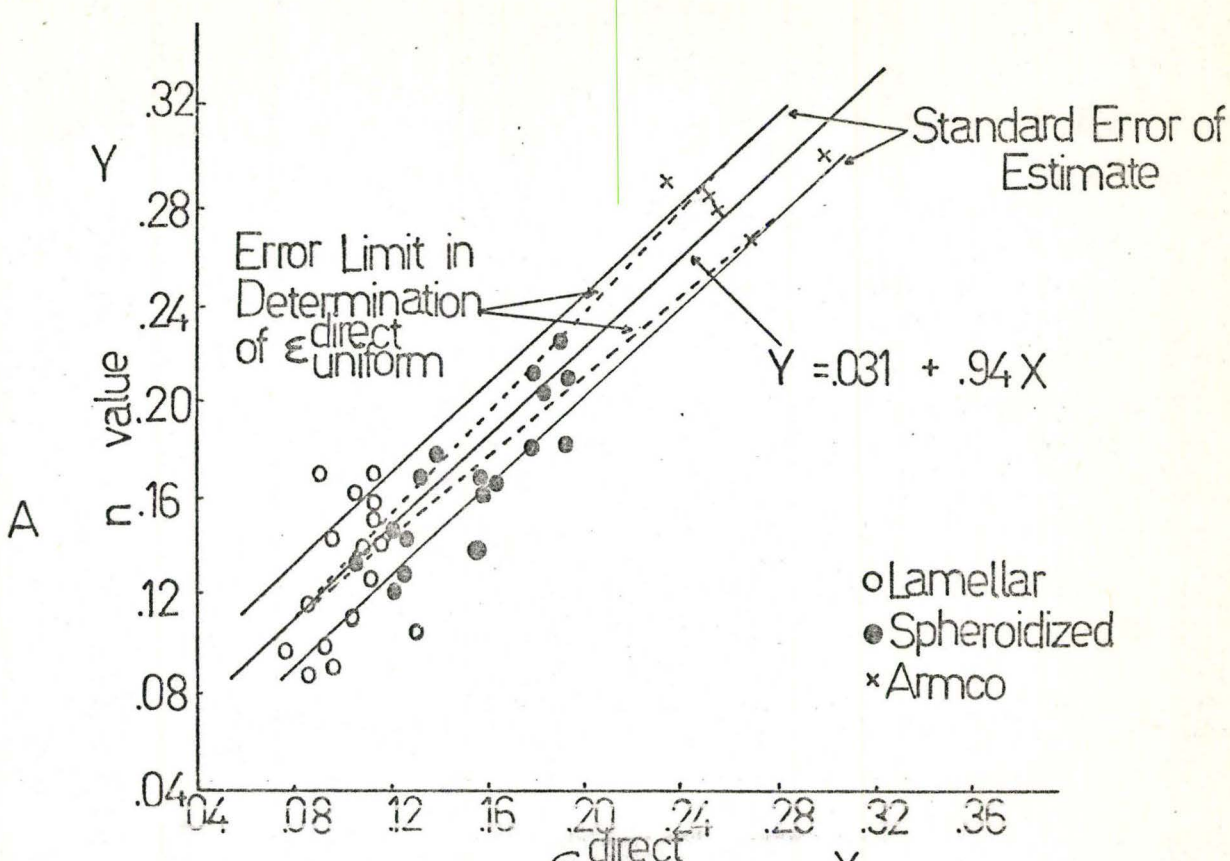

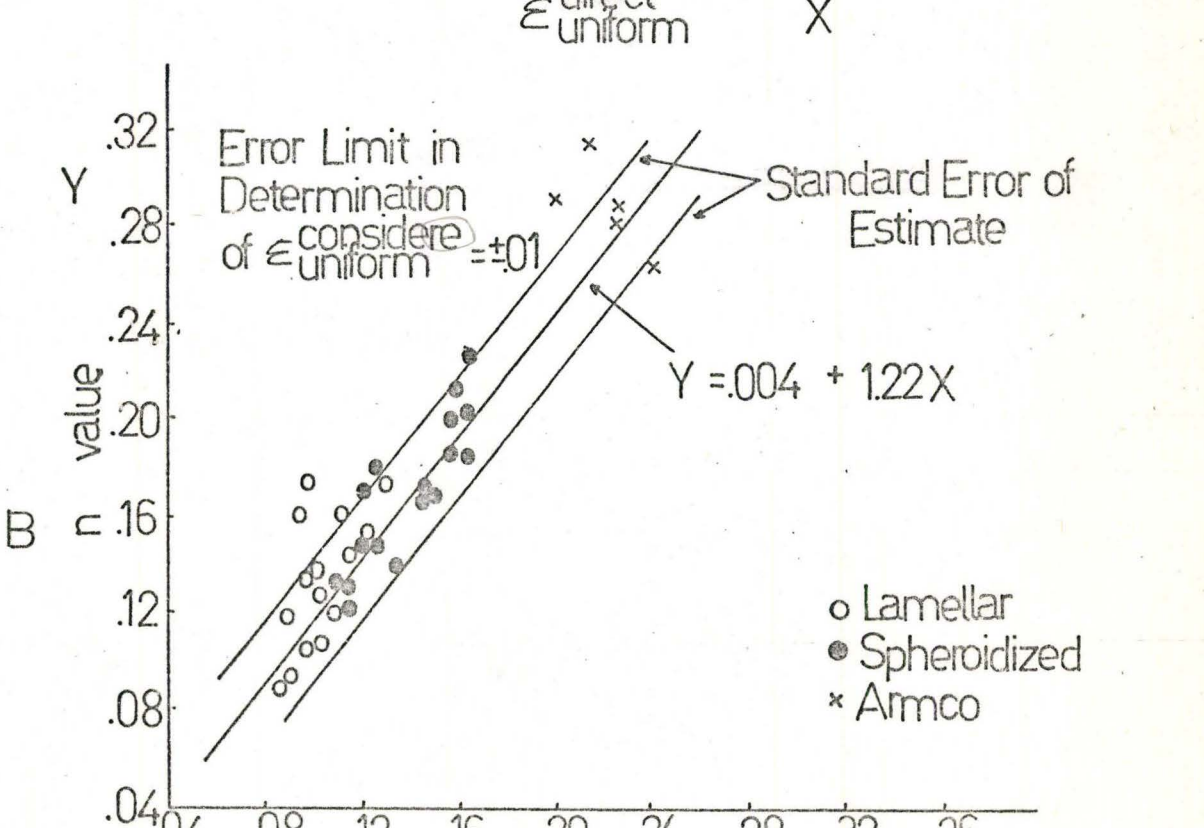

Fig. 27: Relation between the work hardening coefficient and the uniform ductility showing they are numerically equal.

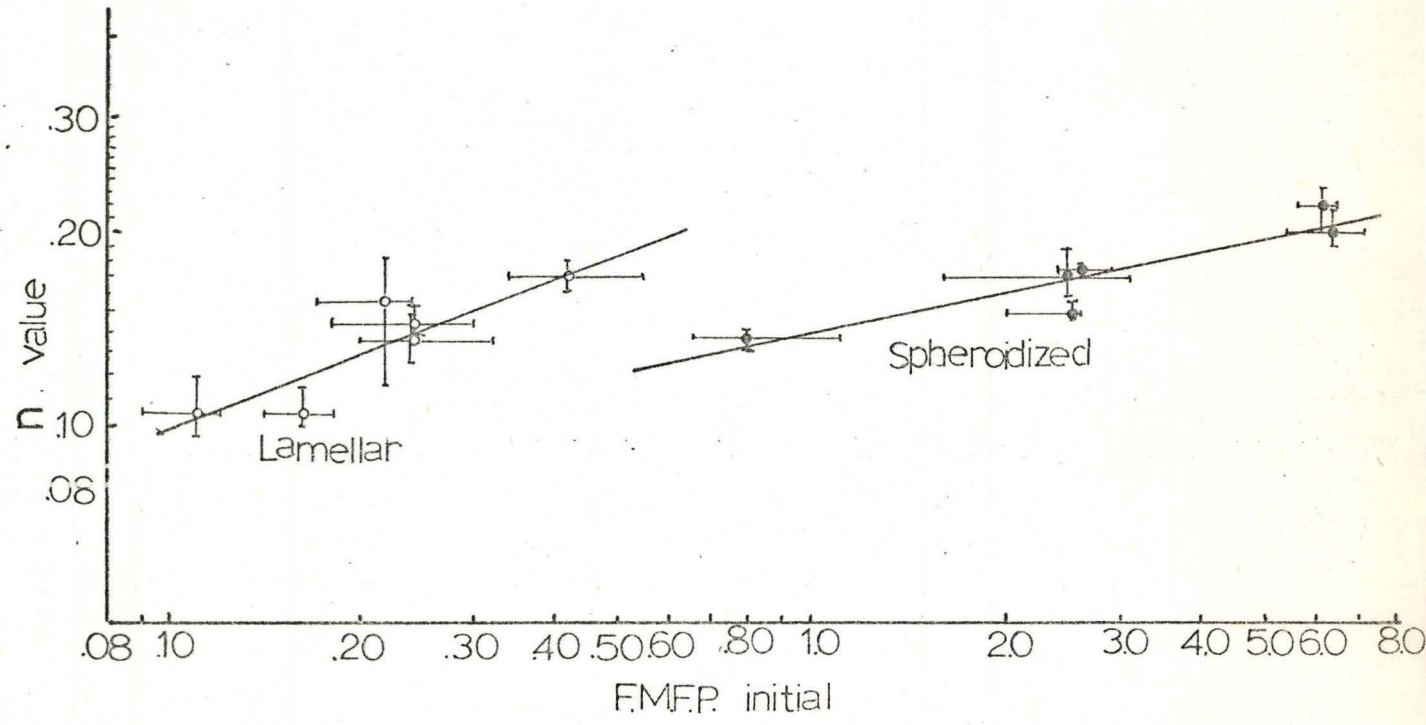

Fig. 29: The dependence of the work hardening coefficient on the F. M. F. P. as $n = B(FMFP)^{b}$.

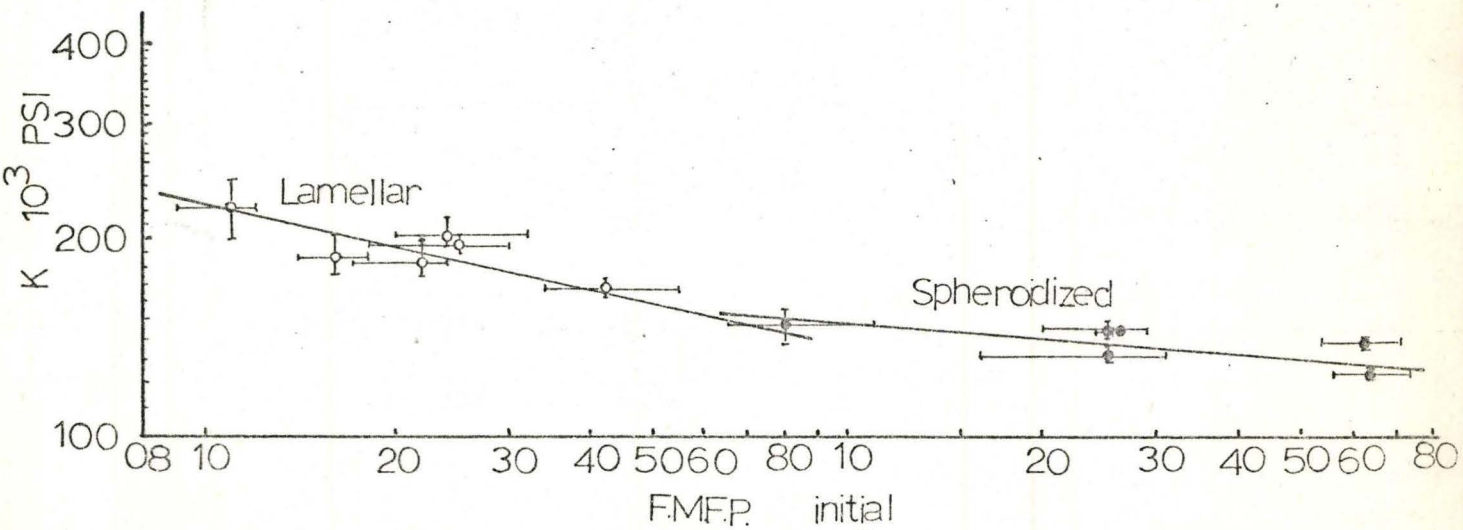

Fig. 28: Pre-exponent constant, K in $\sigma_{f1} = K\varepsilon^{n}$ as a function of (F. M. F.P) assuming $K = A\,(F.M.F.P.)^{n}$

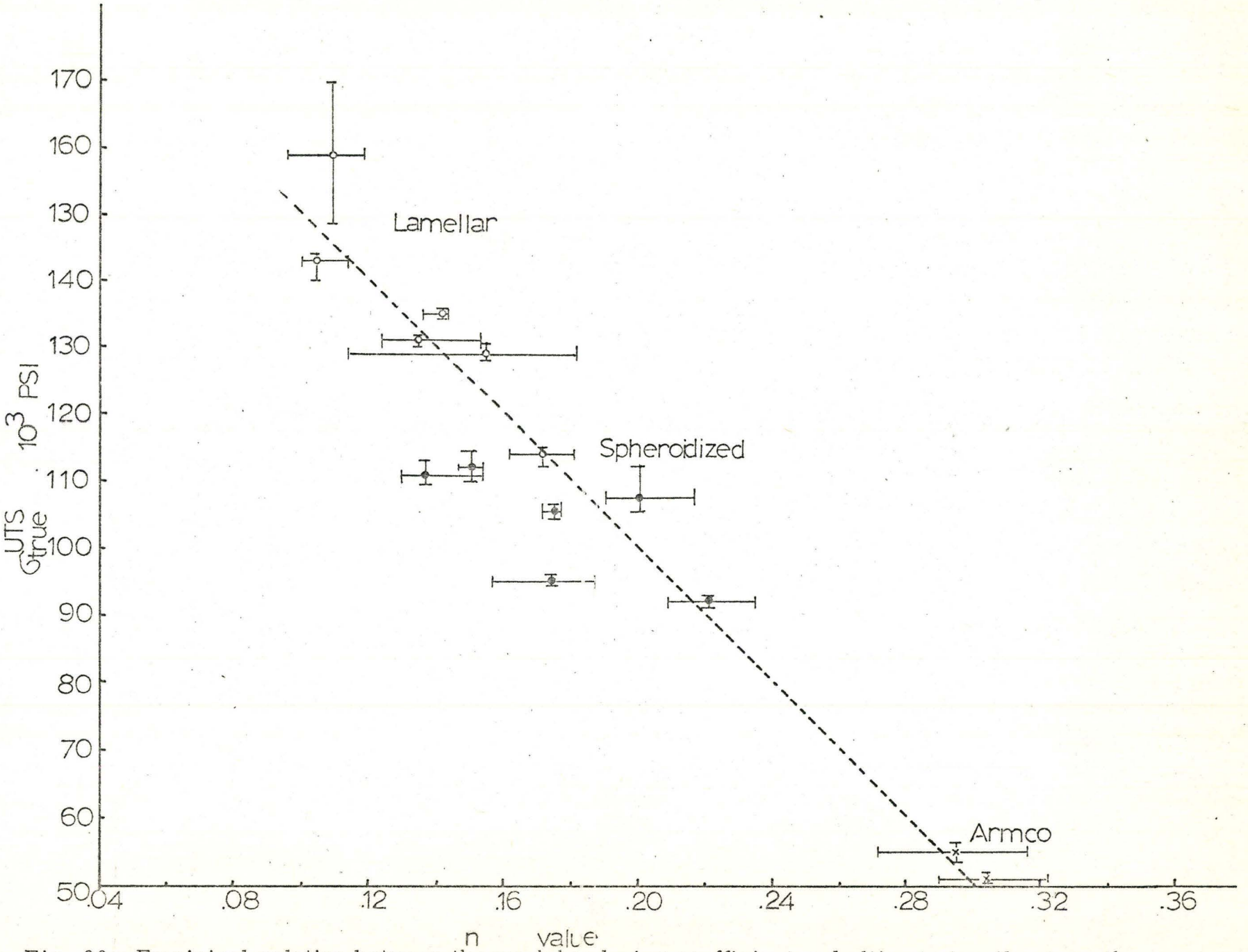

Fig. 30: Empirical relation between the work hardening coefficient and ultimate tensile strength.

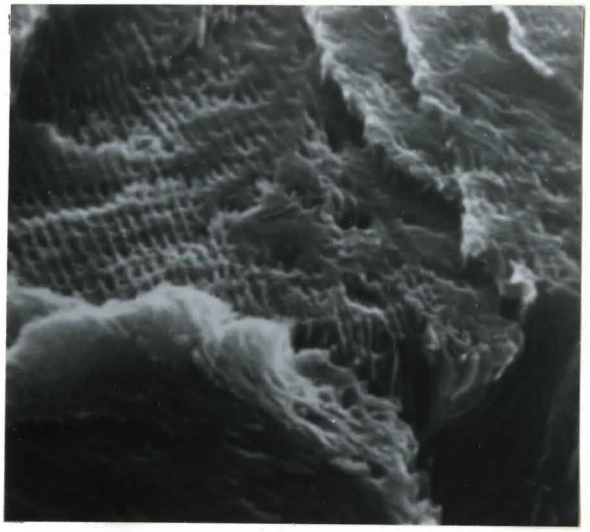

2.3 microns

Fig. 31
LA, Tensile tested at R. T., impact fracture at -196°C and etched

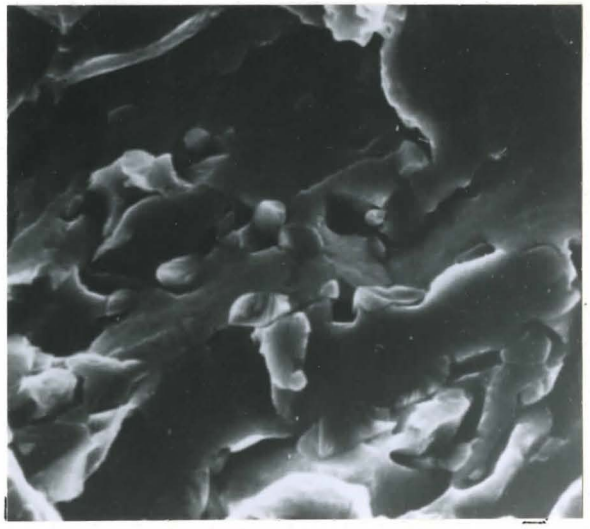

4.9 microns

Fig. 32
SF, Tensile tested at R. T., impact fractured at -196°C and etched

Fig. 31 and 32: Scanning electron micrographs of fractured surface in a method proposed by Tanaka et al.

Fig. 33

LG, Longitudinal
Deformed up to the uniform extension at R. T., polished and etched.

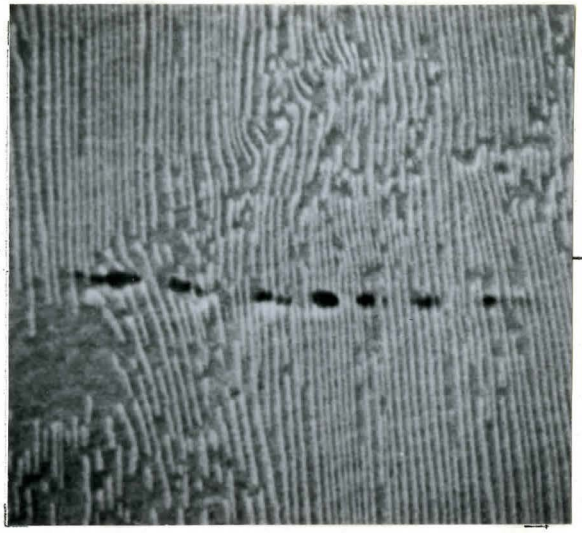

9.2 microns

Tensile Direction

Fig. 34

SF, Longitudinal
Deformed up to the uniform extension at R. T., polished and etched.

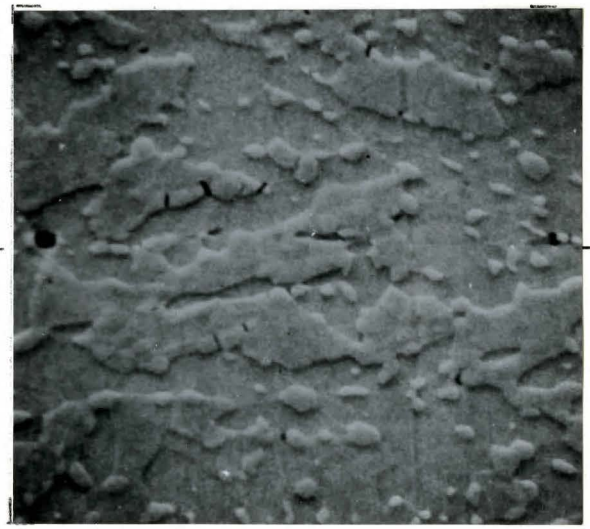

6.4 microns

Fig. 33 and 34: Scanning electron micrographs after the uniform extension in lamellar and spheroidized steels showing some voids left.

A

Armco B, Longitudinal
Deformed up to the uniform
extension at R. T.,
polished and etched

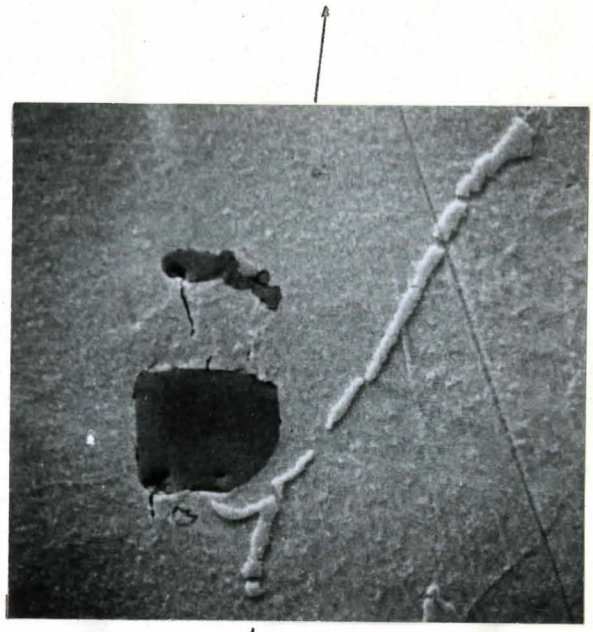

16. microns

Tensile Direction

B

Armco B
The same as above

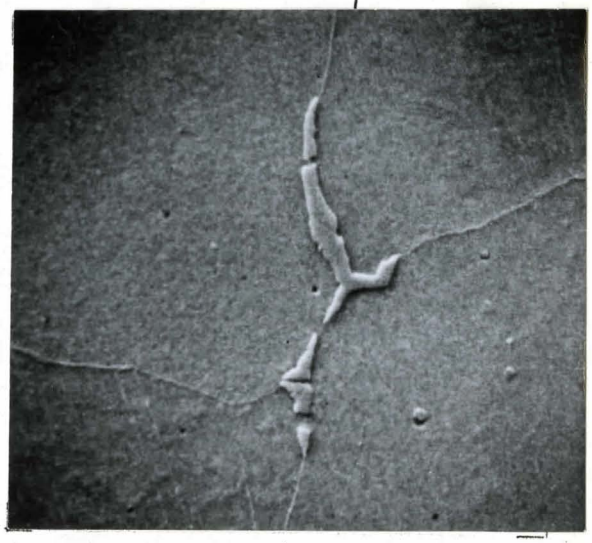

16. microns

Fig. 35: Scanning electron micrographs of fractured cementite particles located at the grain boundary leaving no void between the fracture surfaces.

Fig. 36: A cementite plate showing steps made by shear slip during uniform extension or thin foil preparation.

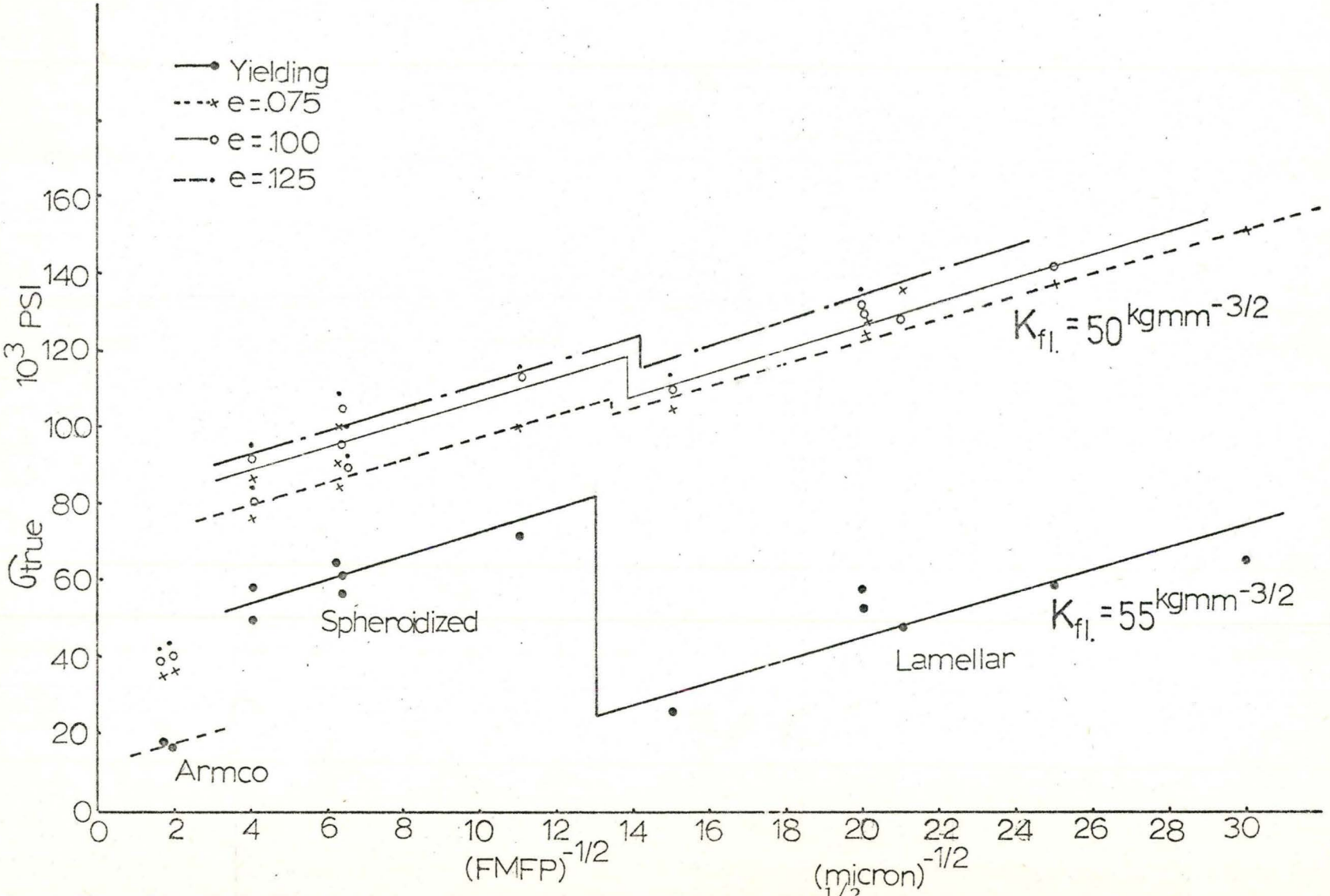

Fig. 37: Hall-Petch plot, σ_{fl} as a function of $(FMFP)^{-1/2}$.

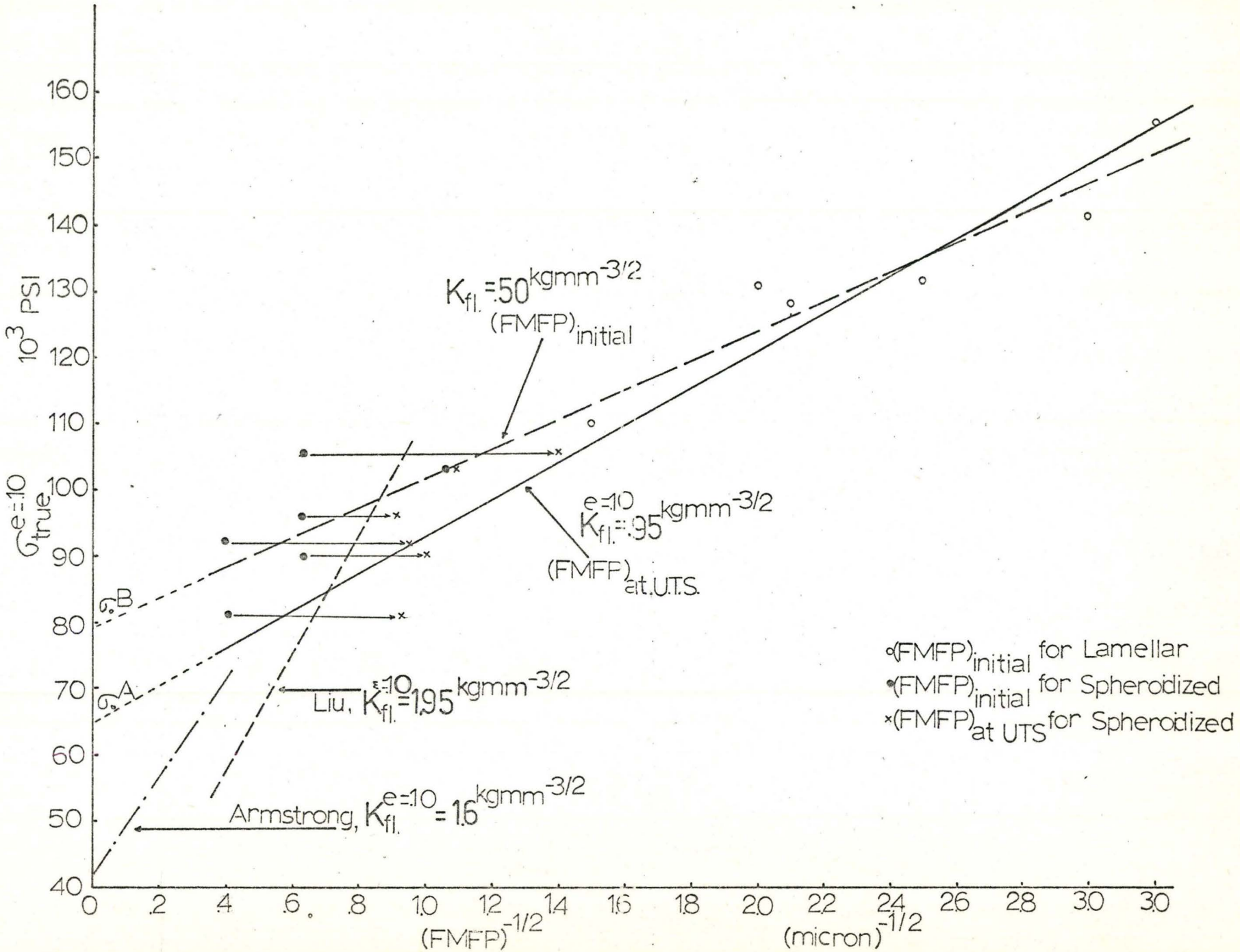

Fig. 38: Hall-Petch plot for σ_{fl} with different microstructural parameters.

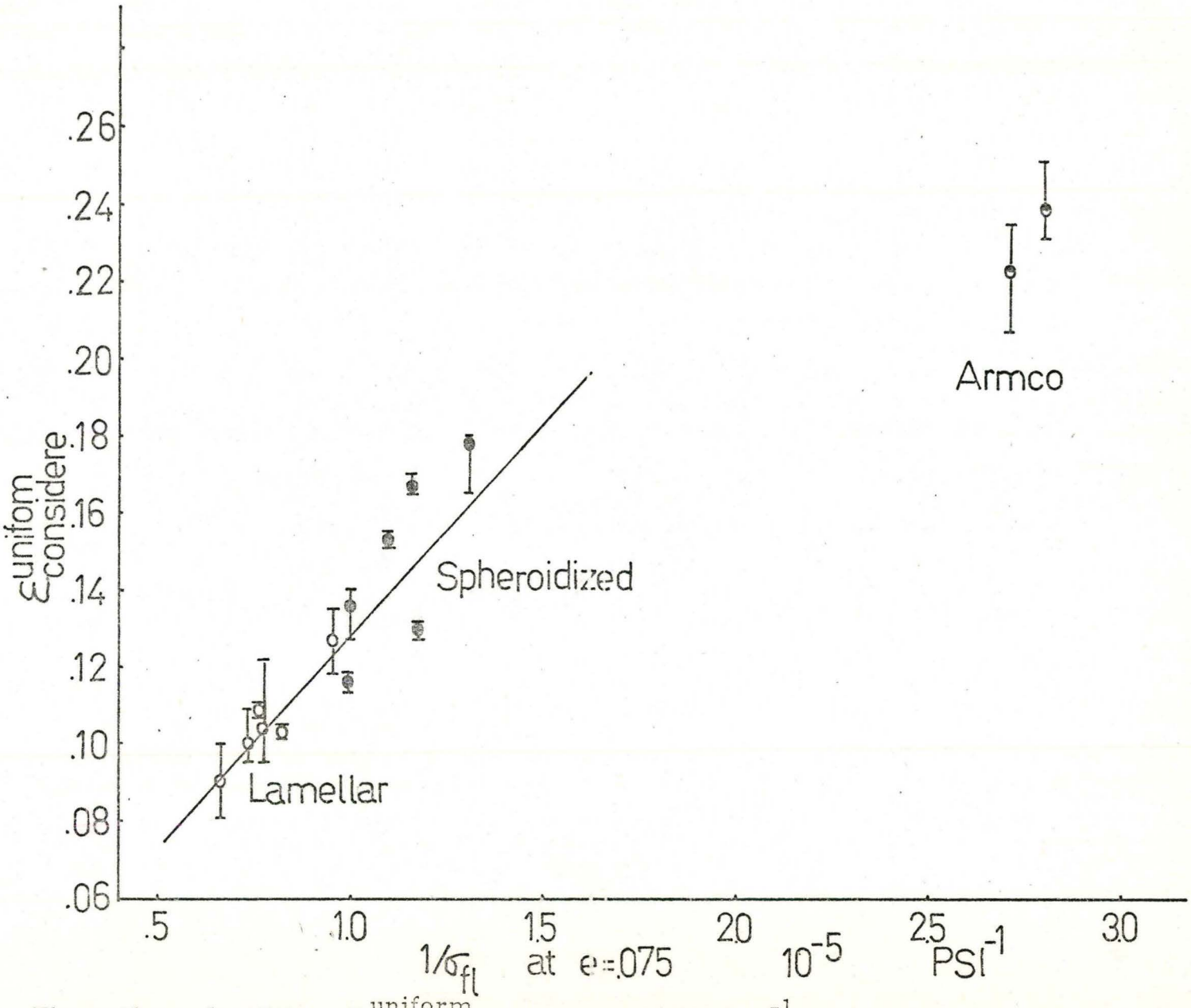

Fig. 39: The uniform ductility, $\varepsilon^{uniform}_{considere}$ proportional to σ_{fl}^{-1}.

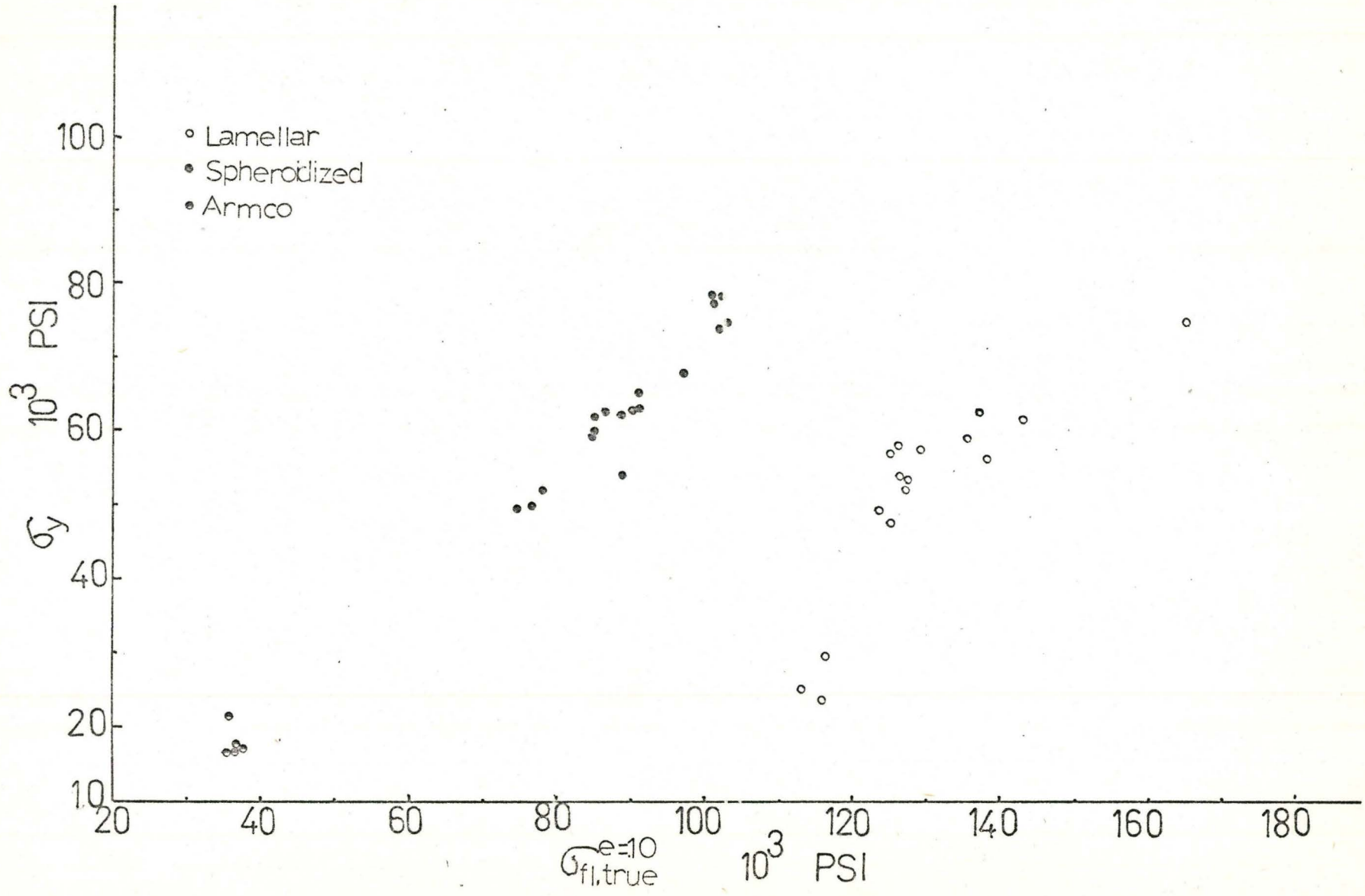

Fig. 40: Empirical relation between σ_y and σ_{fl}.

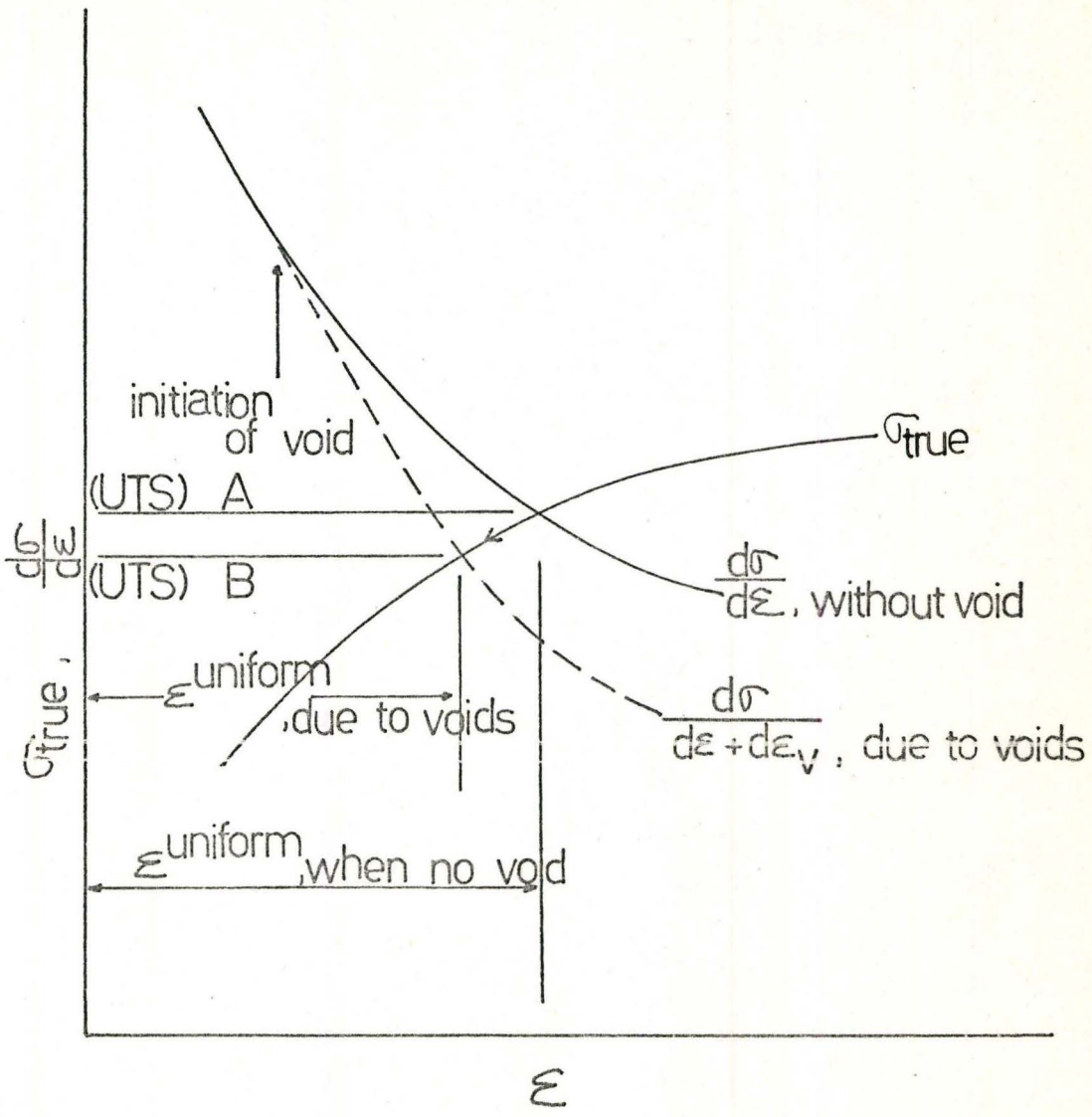

Fig. 41: A schematic Representation of change of ε uniform due to existence of voids.